International Journal of Fatigue 134 (2020) 105484

Contents lists available at ScienceDirect

International Journal of Fatigue

journal homepage: www.elsevier.com/locate/ijfatigue

Waveform and frequency effects on corrosion-fatigue crack growth behaviour in modern marine steels

Victor Igwemezie[a,b], Ali Mehmanparast[a,*]

[a] Offshore Renewable Energy Engineering Centre, Cranfield University, England, UK
[b] Materials and Metallurgical Engineering Department, Federal University of Technology, Owerri, Nigeria

ARTICLE INFO

Keywords:
S355 steel
Corrosion-fatigue
Sinewave
Hold-time
Seawater
Microstructure

ABSTRACT

The primary focus of this work is to investigate the sensitivity of cyclic waveform, frequency (*f*), load level and microstructure on the corrosion-fatigue crack growth rate (CFCGR) in modern normalised-rolled (NR) and thermomechanical control process (TMCP) ferrite-pearlite steels in the Paris Region of the da/dN vs. ΔK log-log plot. Constant amplitude sinewave (*si*) and trapezoid waveform (generally referred to here as hold-time (*h-t*)) were used under frequencies of 0.2 Hz, 0.3 Hz and 0.5 Hz and stress ratio of 0.1. Comparison is also made between the crack path in the S355 TMCP steel under *si* and *h-t* in seawater (*SW*). The role of microstructure in retarding or accelerating fatigue crack growth in *SW* is also discussed. Experimental results showed that the CFCGR corresponding to the *si* is higher than that of the *h-t* for all the load levels and frequencies examined. It was observed that reduction in the *f* and fatigue load level increased the CFCGR for the *h-t* but had little effect on the *si*. Generally, *f* in the range 0.2–0.5 Hz had little effect; and for a given *f* an increase in load led to a reduction in the CFCGR, in the Paris Region (PR) for both *si* and *h-t* in *SW*. Under both *si* and *h-t*, the CFCGR in the TMCP steels (e.g. S355G8 + M, S355G10 + M) is lower than that of the normalised steels (e.g. S355J2 + N). Metallurgical analyses on the fractured surface of corrosion-fatigue specimens show that the main active crack tip blunting process is the primary factor controlling the CFCGR of steel at high stress intensity factor range (SIFR) and low *f* in *SW*. The results obtained from this study have been discussed in terms of the potential impact on the structural design and integrity of offshore wind turbine foundations.

1. Introduction

Steel structures in a dynamic service environment degrade with time due to fatigue. Offshore engineering structures, such as wind turbines (WTs) are subjected to cyclic loading conditions due to constant exertion of wind, wave and currency forces. The initiation and propagation of cracks in these structures could lead to catastrophic failure at loads far less than the yield stress of the material. The fatigue crack initiation and fatigue crack growth (FCG) are accelerated by the seawater (*SW*) environment, i. e., the combination of a corrosive environment and fatigue phenomenon is found to be more detrimental than each of them acting separately. This simultaneous action of cyclic load and chemical attack is commonly referred to as corrosion-fatigue (CF) and it is found to be an important failure mechanism in offshore structures [1,2]. The structural integrity design for such structures aims to ensure that they carry the applied loads during operation without any macro-scale failure throughout the lifespan. For this reason, it has become a common research subject to experimentally measure the FCG under a given stress condition.

Corrosion is both time- and temperature-dependent [3,4]. Two factors that are known to control the extent of corrosion damage contribution to the FCG behaviour of steel are the rate at which the corrosion is occurring, and the time available for the corrosion damage to occur per cycle. In a CF study [5], these two factors have been used to explain the acceleration of crack propagation rates with decreasing test frequency (*f*) under constant temperature. Although experimental investigations have been previously conducted by researchers to characterise the corrosion-fatigue crack growth (CFCG) behaviour of various materials used in offshore structures [5–14], the CFCG behaviour in modern steels used in the design of offshore wind turbine (OWT) foundation structures under various waveforms and frequencies is largely scarce. The sensitivity of the corrosion-fatigue crack growth rate (CFCGR) to *f*, load level and waveforms is pertinent in predicting correctly the lifespan of these support structures under forcing conditions. Hence, accurate characterisation of CFCGR in these structures in direct contact with the *SW* (i.e. in the absence of corrosion protection) could enable more efficient inspection, maintenance and a potential life extension.

* Corresponding author.
E-mail address: a.mehmanparast@cranfield.ac.uk (A. Mehmanparast).

https://doi.org/10.1016/j.ijfatigue.2020.105484
Received 21 October 2019; Received in revised form 12 January 2020; Accepted 14 January 2020
Available online 25 January 2020

Nomenclature

BFS	Back face strain
CF	Corrosion-fatigue
CFCGR	Corrosion-fatigue crack growth rate, (da/dN)
CFCG	Corrosion-fatigue crack growth
FCG	Fatigue crack growth
DSM	Ductile striation mechanism
FCGR	Fatigue crack growth rate
PS	Present study
SIF	Stress intensity factor
SIFR	Stress intensity factor range (ΔK)
TMCP	Thermomechanical control process
NR	Normalised-rolled
OWT	Offshore wind turbine
SEM	Scanning electron microscopy
EDX	Energy-dispersive X-ray Spectroscopy

1.1. Fatigue loading and the operational frequency range of offshore wind turbine support structures

For OWTs the external environmental effects such as wind and wave forces result in the development of stresses in the support structures, which are dominantly made of monopile structures [15]. The magnitude of these cyclic stresses directly determines the functionality and lifespan of the OWT. The assessment of the first natural *f* of the OWT and *f* distribution (or the eigenfrequencies – i.e. range of frequencies within which the WT can vibrate) is a very important part of WT design. The natural *f* of a WT is the *f* with which the system oscillates during normal operating condition. Fig. 1(a) shows that forces acting on a typical WT support structure are axial loads, lateral loads and bending moments. Torsional loading is sometimes considered too [16].

The bending moments vary cyclically due to operational rotation of the blades and the magnitude increases with the rotor diameter [20]. Among these forces, dead loads, the meteorological and oceanographic (MetOcean) conditions are considered to be the most significant loads acting on the structure [21]. Dead loads are self-weight of: the pile, the transition piece - if used, the tower and the turbine (rotor – hub and blade, and nacelle). MetOcean loads are wind, waves and current. Fig. 1(b) shows the wind shear and wind induced wave profile along the support structure of an OWT. The wind speed changes with time and also with changes in the turbine height above the sea level or ground surface as shown [18]. The variation in wind speed is obviously a random or stochastic process and the stochastic nature of fatigue loading on WT structures is not easily defined [16]. Stochastic loads cannot be predicted to occur with a certain magnitude at a given time. This makes it difficult to simulate such conditions in the laboratory. This perhaps has been the reason for the common use of the constant amplitude stress range in fatigue experiments. As a very simplified approach, we can assume that the wind loading on a WT occurs in three stages – the rising stage, 'dynamically steady' stage and relaxation stage. A simplistic view of this idea is shown in Fig. 2(a) with associated gust loading and turbulence. This waveform is adapted from a typical wind loading spectrum acting on aircraft wings [22]. In reality, these three stages will vary continuously and randomly to build up the wind spectrum without a well-defined reference line. Under our assumption and for experimental purposes, we may approximate the wave spectrum of Fig. 2(a) to a hold-time waveform (*h-t*) as shown in Fig. 2(b). Varying the maximum load (P_{max}) or maximum stress intensity (K_{max}) in laboratory experiments may provide a simple way of measuring the damaging contributions of different turbulence peak ranges.

The thrust force, P_1 in Fig. 1(c) is the lateral wind force acting on the rotor (often taken to act at the hub) of the turbine from the rotating blades [23]. Also shown is the wind load on the tower P_2, wave and current loads P_3 on the substructure as illustrated by [18]. Wind force or moment due to wind loading on the tower structure is small compared with the magnitude of the thrust forces acting on the rotor during operation. Hence, the predominant external fatigue problem on OWTs comes from wind loads that has longer moment lever arms (Fig. 1(c)), acting on the hub and impacting the greatest bending moment ($M = P_1 * Y_1$) on the support structure during normal operation [20].

The frequencies of the loads that are commonly taken into considerations are those of the wind and wave spectra, and operational intervals of the rotor. The primary excitation *f* due to the rotational speed of the rotor is commonly called the *1P*. For modern OWTs, it is reported that the rotor speed under normal operation is typically about 7–12 revolutions per minute (rpm), which corresponds to *1P f* of 0.12–0.20 Hz [24]. The second excitation *f* of OWT occurs due to the creation of wind shade by the WT tower. Any time a single blade of the rotor passes across the wind shade of the vertical tower there is reduction of the wind loading on the tower causing additional cyclic load on the support structure at the *f* equal to *1P* times the number of blades. Thus, *3P* is the blade passing *f* for a 3-bladed WT (see Fig. 1(b)). This implies that if the rotor completes 6 rpm, the *1P f* is 0.1 Hz while the 3P is 0.3 Hz. Regarding wave loading (which is often produced by wind), the common frequencies in the North Sea are in the range 0.04–0.10 Hz

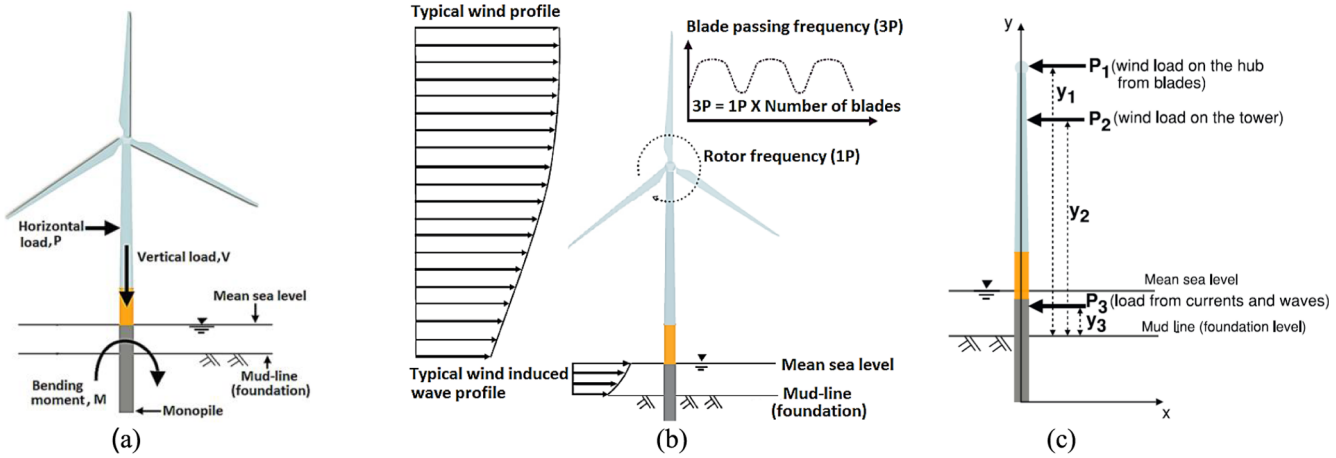

Fig. 1. Fatigue loads on WT (a) Nature of loads on a monopile supported WT [17] (b) wind shear and wind induced wave profile - the main external dynamic and cyclic loads acting on a typical OWT [18,19] (c) position of the thrust force P_1 on the hub of the rotor.

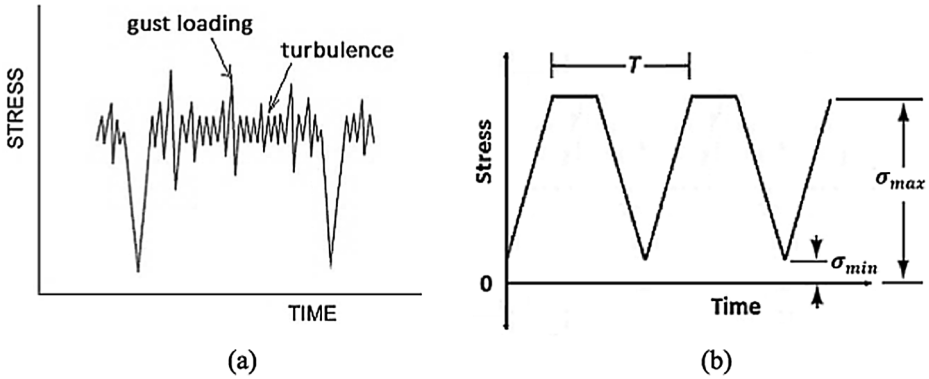

Fig. 2. Experimental waveforms and loading parameters: (a) A simplistic illustration of wind loading stages on a WT, (b) & (c) hold-time and sine waveforms used in the present study, (d) & (e) programme waveforms.

[17]. Many of the studies on CFCGR in marine environment used a *f* of 0.1 Hz and temperature range of about 4–10 °C. The goal of these studies has been to simulate offshore conditions and obtain fatigue data for application in offshore Oil & Gas production and exploration platforms. This would then enable extrapolation of the laboratory data to field structures. For the gust wind, using the Davenport *f* spectrum model, the dominant *f* of a gusty wind is reported to be about 0.02 Hz [25], lower than that of the waves of about 0.1 Hz.

Generally, during the design of commercial OWTs, *f* of the support structure between *1P* and *3P* is assumed [26]. This *f* condition of the WT is referred to as soft-stiff design [18]. Fig. 3 shows a typical design *f* range for commercial and reference WTs. The *f* range is between about 0.2–0.35 Hz for the *Soft-Stiff* region. Table 1 shows the 1P and 3P frequencies for some theoretical and commercial WTs. This implies that fatigue experiments of practical significance for many of the commercial WTs in the soft-stiff condition should be carried out in the range of, say, 0.16–0.54 Hz [26]. This informed the frequencies used in this research. It is pertinent to note that there is no study in the literature that examines the *f* effects on CFCGR behaviour of modern structural steels employed in the fabrication of these monopiles.

1.2. Previous studies on frequency and waveform effects on corrosion-fatigue

Corrosion is a time-dependent material degradation mechanism. In the CF process, the loading *f* and the waveform of the load cycle are expected to have some potential effects on the crack growth behaviour of steel in a corrosive environment. Many studies have shown that the fatigue crack growth rate (FCGR) is sensitive to the waveforms in a *SW* environment but not in air. It has been shown in previous studies found in the literature that for the stress ratio (R) in the range of 0.1–0.85 and *f* in the range 0.005–50 Hz , waveforms have little or no effect on the FCGR in the ferrite-pearlite steels in air [27–31,27,32,33]. However, these studies have reported that the CFCGR in *SW* is sensitive to the loading waveform due to the difference in the deformation mode at the crack tip (crack tip geometrical difference). These studies have shown that under anodic dissolution, the amount of material dissolved at the vicinity of the crack tip within one cycle of loading was the same for sinusoidal (*si*), positive sawtooth (*p-s*), negative sawtooth (*n-s*) and square (*sq*) waveforms.

A continuous loading pattern was reported to give accelerated CFCGR. According to these studies, the CFCGR of the *p-s* was found to be higher than that of the *si* waveform and the rates for the two waveforms were higher than that of *n-s* and *sq* waveforms in free corrosion test conditions. It was also established that for the case of the *sq* waveform, holding for 0.1 s and 0.9 s at maximum load had little influence on the CFCGR. Consequently, the waveform crack growth rate difference was attributed to the continuous deformation of the crack tip material.

Atkinson and Lindley [29] studied FCGR in Fe-C-Si-Mn structural

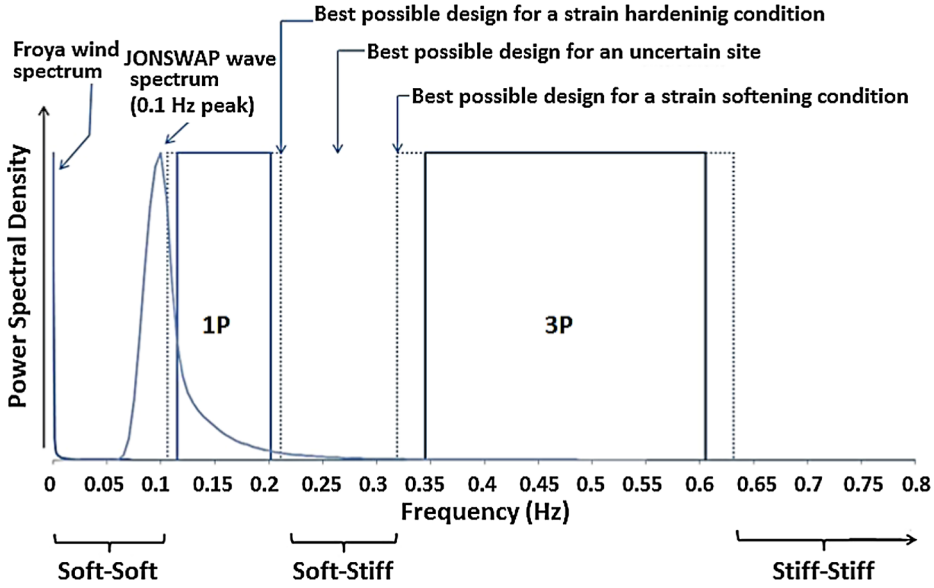

Fig. 3. The 1P and 3P frequency range for 3 bladed NREL standard 5 MW WT [27].

Table 1
1P and 3P frequencies for some operational and reference offshore WTs.

Name	Rotor Freq. Range (1P) [Hz]	Blade passing Freq. Range (3P) [Hz]	Ref.
Vestas V66 2 MW turbine	0.18–0.41	0.54–1.23	[18]
Vestas V90 3 MW turbine	0.14–0.31	0.42–0.90	[18]
Siemens SWT-3.6(MW)-107	0.08–0.22	0.24–0.66	[18]
Vestas V120 4.5 MW	0.17–0.25	0.50–0.75	[34,35]
NREL 5 MW WT	0.12–0.20	0.35–0.60	[17]
DTU 10 MW RWT	0.10–0.16	0.30–0.48	[36]
3 MW Sinovel WT	0.14–0.32	0.41–0.95	[37]

steel designated BSI501-213-32A [29,38] under triangular waveform (*tr*) in air, distilled water and natural lake water at temperatures between 25 and 30 °C and pH 6.0. The range of frequencies used for the *tr* tests was 0.005–1 Hz. They found that FCGR in both distilled water and lake water were similar at a very slow loading rise-time of about 100 s. The increase in the FCGR by the water environment was found to depend on the rise-times. A rise-time less than 1 s had a negligible effect. They also carried out the experiment in room-temperature lake water using *sq*, *p-s* and *n-s* at a *f* of 0.01 Hz. The FCGRs of the *p-s* and *tr* were found to be the same at the same rise-time. The environment was found to have no effect on the FCGRs for the fast-rising *sq* and *n-s* at the same 0.01 Hz. Hence, they suggested that rise-time rather than total cycle time controlled the FCGR for the steel in water. They reported that *n-s* and *sq*, which have very rapid rise-times (i.e. period of increasing tensile load) of the fatigue cycle, did not increase the CFCGR at frequencies as low as 0.01 Hz. Also reported was that holding at maximum load in the *SW* for up to 10 min did not affect the FCGR at room temperature and at high cyclic frequencies the FCGR in the *SW* was similar to that in air.

Austen [39] studied CFCGR of EN24 steel [39–41] in distilled water under *tr*, *p-s*, *n-s* and *sq*, at R = 0.25 and *f* = 5 Hz. From the plot of *da/dN* vs. ΔK presented in his work, the CFCGRs under *p-s* and *tr* were generally the same and were slightly above those of *n-s* and *sq* in the ΔK range of about 15–28 MPa√m within the Paris Region. Above the 28 MPa√m, the CFCGRs of all the waveforms became generally the same; though, the CFCGR of the *n-s* was somewhat the lowest. They also studied CFCGR in a high strength martensitic steel designated 300 M [42] using a R = 0.5 and *f* = 0.45 Hz. The waveforms employed were *si*, *tr* and *sq* and the environment was distilled water. His result shows that the CFCGR in the 300 M steel increased thus; *si* > *tr* > *sq*. For the *sq*, *f* above 1 Hz and holding at the P_{max} in the range 0.01–0.5 s, had a negligible effect on the CFCGRs in the Paris Region. This implies that the *si* is the most damaging waveform, while the CFCGR by the waveform that allows substantial time for corrosion process to occur at the crack tip (e.g. *sq*) or the waveform with very short rise-time (e.g. *sq*, *n-s*) was the least. Generally short rise time and increase in the *f* of the waveform decreased the CFCGR towards the air value in his study.

Nakasa and Takei [10] studied CFCGR in JIS SNCM439 steel [10,43] quenched and tempered at 200 °C and 500 °C. They reported that CFCGR was higher in the *sq* load waveform than *p-s* for steel with high sensitivity to delayed failure. The sample tempered at 500 °C exhibited delayed failure under static stress and higher CFCGR under *p-s* compared with the case of *sq* waveform. They suggested that stress rise time and hydrogen concentration control the crack growth in corrosion-fatigue. This implies that the interaction between the crack tip and hydrogen atoms controlled the crack growth mechanism.

Bhuyan et al. [44] studied the effect of waveform on CFCGR in a steel manufactured to CSA G40.21 M 350 wt [45] in air and *SW* under constant amplitude loading. The pH of the *SW* was in the range 7.25–7.55 while the temperature was in the range 0–21 °C in seawater and −15 to 4 °C for the tests in air. The tests were carried out using *si* and sawtooth waveforms. They reported that CFCGR in seawater was on average 2.7 times higher than that in air for R = 0.1, *f* = 0.05 Hz and in temperature range of 0–4 °C. They proposed that CFCGR decreased and tended towards air value as the *f* was increased from 0.05 Hz to 0.5 Hz at R = 0.1 and increased by a factor of 2.3 as the *f* was decreased from 0.5 to 0.05 Hz. For the air test, the FCGR was almost unaffected in the temperature range of −15 to 4 °C and was generally not influenced by the load ratio variation in the range of 0.05–0.3.

In a study conducted by Thorpe et al. [5], the R and *f* were found to have no effect on FCGR in air. Similar results were obtained from the test with *tr*, *p-s* and *si* waveforms. They also showed that the CFCGR increased as test *f* is decreased, and R increased. Appleton [46] studied the CFCGR in BS4360 grade 50D [26,47] steel in 3% NaCl at room temperature and found that there was no difference in the CFCGR for the tests done at 0.05 Hz, 0.17 Hz and 1 Hz up to about a SIFR of 18 MPa√m. However, above this value, the CFGCR test at 0.17 Hz increased steadily above that of 1 Hz. A large decrease in the CFCGR was seen at the test performed at 5 Hz. In general, the effect of seawater started decreasing steadily from 1 Hz upwards towards that of air test values. Moreover, the results showed that for the 0.17 Hz tests, there was no significant change in the CFCGR curve in the R range of 0.1–0.7. Appleton [46] also performed tests at other waveforms. The additional waveforms were *tr* and *sq* shape at 0.17 Hz. No difference in CFCGR was observed between *si* and *tr* waveforms.

Barsom and Rolfe [27] studied waveform effect on the FCGR in a 12NI-5Cr-3Mo maraging steel [48] and the test was performed in air and 3%NaCl and they compared the effect of *si*, *tr*, and *sq* waveforms loadings. The effect was investigated for frequencies in the range of 0.1–10 Hz. The results showed that similar FCGR results were obtained in air for the three waveforms. In other words, waveform has no effect on crack growth in the air. In the 3%NaCl, the CFCGRs of the *sq* waveform and *n-s* were the same and slightly higher than the air data, by a factor of 1.1. For the *si*, *tr* and *p-s* waveforms the CFCGRs were similar to each other and significantly higher than the FCGR in air by a factor of 3. Barsom [49] also showed that there was no significant difference in FCGR for tests under random-sequence and ordered-sequence load fluctuations.

Wand et al. [50] studied the influence of waveform on CFCGR of iron with yield stress, tensile strength and elongation of 150 MPa, 295 MPa and 42% respectively in 3.5%NaCl. The test *f* was 0.1 or 1 Hz and R = 0. The waveforms *si*, *p-s*, *n-s* and *sq* waveforms were investigated. They found that the *p-s* and *sq* loading waveforms have very little or no effect on the FCGR in air. This result tends to confirm that waveform generally has no effect on the rate at which a fatigue crack grows in steel in air.

Knop et al. [51] studied the effect of cycle *f* rise-time on CFCGR of a high-strength steels. They also presented the effects of drop-times and hold-times at maximum and minimum loads on the CFCGRs. They found that FCG at the Paris Region is generally caused by plastic blunting and that the crack length increased during the rising of the load towards the cycle peak for each load cycle. They reported that the difference between crack growth in inert and embrittling environments was that less crack tip blunting occurred in the embrittling environment due to localisation of deformation slips and this resulted in increased crack growth rate. They suggested that CFCGR depended on the concentration of hydrogen adsorbed at crack tips and at tips of nanovoids

ahead of crack fronts. They concluded that crack growth is enhanced under increasing rise-time and that longer drop-times and longer hold-time at maximum and minimum loads are likely to have the same effect when the rise-time is short. In their study, the rise-time period was from 1 to about 10 s and the crack growth rate within this time range depended on the SIFR.

1.2.1. Research motivation for the present study

In all the studies reviewed above, there is no explicit comparison of waveform effect under the same *f* and constant load ratio for subgrades of a particular grade of steel with differing microstructures. There is also limited evidence of the cracking micrographs and in-depth investigation of contributions of the microstructural phases under these waveforms in the CF tests. The influence of waveforms other than *si* on CFCGR for the steels used for OWT foundation design is non-existent, at least to the extent of information available to the authors. The previous review of the existing studies on *f* and waveform effects on corrosion-fatigue has revealed that CFCGR is sensitive to waveform and *f*. This sensitivity to waveform underscores the need to perform CFCGR tests based on real operational loading conditions. It is then desirable to perform tests under realistic loading modes in order to enable more efficient design, inspection planning and life prediction of OWT support structures. However, the loading condition on a commercial OWT is highly stochastic as noted in Section 1.1. The goal of the present study (*PS*) is to; (1) determine the effect of two different types of waveforms, sinewave and trapezoid waveform with hold-time at the maximum load, as well as various frequencies on CFCGR in *SW*. The choice of hold-time has been explained in Section 1.1. And (2) to identify the more damaging of the two waveforms, hence the most conservative analysis that can be employed in the life assessment of OWT monopile foundations.

In general, this paper presents new sets of experimental results on the effect of *f*, waveform and load level/K_{max} on the CF behaviour of normalised-rolled (NR) and thermomechanical control process (TMCP) ferrite-pearlite steel subgrades of S355 which are widely used in the fabrication of modern offshore structures, including OWT monopile foundations. The waveforms considered in this study are sinewave and trapezoid with hold-time and the experiments were conducted under frequencies of 0.2 Hz, 0.3 Hz, 0.5 Hz at the fixed stress ratio of R = 0.1 for comparison purposes. The experiments performed in this study are expected to assist towards a more reliable assessment of CF in OWT foundations in free-corrosion conditions in a marine environment.

2. Material selection and specimen preparation

Traditionally, BS4360 Grade 50D was widely used in the design of offshore structures. The BS4360:1990 code has been withdrawn and replaced with EN10025 S355. In recent years, European Standard EN10025 S355 has become the main structural steel typically in use for OWT structures [38,47,52]. Different sub-grades of S355 are selected for use in offshore applications, including monopiles. The equivalent grade of BS4360 Grade 50D is S355J2 + N. The EN10025 choice for offshore application and the equivalent EN10225 and BS4360 steels are shown in Table 2. The materials S335G8 + M, S355G10 + M and S355J2 + N were investigated in this study. The first two are TMCP steels, while S355J2 + N is NR. Table 3 gives the chemical and mechanical properties of these sub-grades of S355 steel.

For the EN10025 in Table 2, 'S' represents structural steel and the sub-grades JR, J0, J2, K2 refers to the steel toughness at a specific temperature using the Longitudinal Charpy V-notch impacts test method. The 'J' denotes the notch impact test performed at; JR: room temp, J0: 0 °C, J2: −20 °C. The simple meaning is that S355JR can withstand an impact energy of 27 J at 20 °C, S355J0 at 0 °C, S355J2 at −20 °C [47]. S355N has impact energy of 40 J at −20 °C while S355NL has impact energy of 27 J at −50 °C [47]. N & NL denote normalised and normalised rolled, weldable fine grain structural steels respectively. For example, S355J2 + N is a structural steel with an impact resistant testing strength of 20 J at a testing temperature of −20 °C (J2) and has been given a normalised heat treatment (+N). For the EN10225, the 'G' denotes the grade that has been vacuum degassed, fully killed and hot rolled to give a fine-grained microstructure. The M refers to the grade that has been thermo-mechanical control rolled (or processed) (TMCR or TMCP).

The FCG behaviour of S355G10 + M in air has been previously characterised by the authors and the results are available in Ref. [26]. The goal of this study is to characterise the FCG behaviour of these subgrades in a free-corroding environment and to examine the effects of hold-time and *f* on the FCGRs. Compact tension C(T) specimens in accordance with ASTM E647 –15 Standard [53] were extracted from the mid-thickness of 90 mm thick plates shown in Fig. 4(a). The specimens were extracted from a distance reasonably away from the as-received steel plate surfaces. Fig. 4(b) shows the 3D schematic of the experimental specimen. The C(T) specimen dimensions are given in Table 4 and a total of 15 CF tests were conducted. As seen in this table, all tests were performed on standard C(T) specimens with a width of $W = 50$ mm and average thickness of $B = 16$ mm. The initial crack length, a_0, (i.e. after pre-fatigue cracking), final crack length, a_f, and loading conditions for each test are presented in the same table. Note that in test IDs, each sample is denoted by material type (e.g. J2N, G8 and G10), followed by the environmental/waveform condition (e.g. S which stands for corrosion-fatigue test with sinewave and H which stands for corrosion-fatigue test with hold-time), the maximum load applied, P_{max}, on the sample (e.g. 9, and 10 kN), and the applied *f* (e.g. F of 0.2, 0.3 and 0.5 Hz). Also included in this table are the loading conditions for each test. All tests were conducted using the same load ratio of $R = 0.1$. All the fatigue tests were conducted in accordance with ASTM E647-15 [53] and BS 7910 [55].

3. Test set-up and crack growth monitoring in seawater

3.1. Seawater test set-up

For the corrosion-fatigue tests, artificial seawater was prepared in accordance with ASTM D1141-98 [56]. The pH of the seawater was maintained in the range of 8.0–8.2. Before the commencement of the corrosion-fatigue tests, pre-cracked specimens were soaked in seawater up to 2 days. During the tests, the seawater temperature was maintained within the range of 7.5–8.2 °C. The CF tests were carried out in a Perspex chamber (see Fig. 5(a)) where the *SW* was circulated around the C(T) specimen by means of a pump at a continuous rate of about 4 L/min.

The volume of the seawater was such that the same chemical conditions and pH range were obtained at the end of each test. The

Table 2
S355 structural steels for marine applications, (a) advanced S355 subgrades (b) Conventional S355 structural steel grades.

Offshore Structural Steel Plates			
(a)		(b)	
European	Typical offshore application	European	British
EN10225		EN10025 Part 2: 2004	BS4360:1990
S355G7 + N	Primary Structure	S355	50A
S355G7 + M	Primary Structure	S355JR	50B
S355G8 + N	Critical Joints	S355JO	50C
S355G8 + M	Critical Joints	S355J2	50D
S355G9 + N	Primary Structure	**S355J2 + N**	50D
S355G9 + M	Primary Structure	S355K2	50DD
S355G10 + N	Critical Joints	S355K2 + N	50DD
S355G10 + M	Critical Joints	S355NL	50EE

Table 3
Chemical compositions and mechanical properties of the examined materials in this study.

Steel Grade	Notation	C	Mn	Ni	Si	Cu	Cr	Mo	E%	YS (MPa)	UTS (MPa)
S355G10 + M (TMCP)	G10 + M (G10)	0.06	1.57	0.33	0.27	0.24	0.03	0.01	38	435	545
S355G8 + M (TMCP)	G8 + M (G8)	0.05	1.52	0.32	0.27	0.24	0.03	0.01	35	447	549
S355J2 + N (NR) [54]	J2 + N (J2N)	0.17	1.54	0.04	0.04	0.08	0.02	–	20	385	531

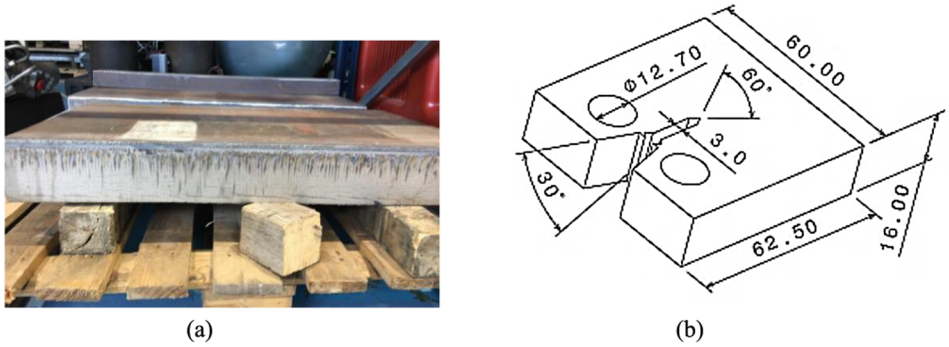

Fig. 4. (a) Steel plates used in this study, (b) 3D schematic of the C(T) specimen design.

Table 4
Specimen dimensions and loading conditions in seawater tests.

#	Test ID.	W (mm)	B (mm)	a_o (mm)	a_f (mm)	f (Hz)	P_{max} (kN)
1	J2N-S10F0.2	50.00	16.00	18.32	28.02	0.2	10
2	J2N-H10F0.2	50.00	16.00	18.55	31.07	0.2	10
3	G8-H10F0.2	50.01	16.02	17.03	33.83	0.2	10
4	G10-S10F0.2	50.0	16.00	21.26	29.11	0.2	10
5	G10-H10F0.2	50.05	16.08	22.37	29.38	0.2	10
6	G10-S10F0.3	50.03	16.05	21.57	29.44	0.3	10
7	G10-H10F0.3	50.03	16.07	21.87	29.73	0.3	10
8	G10-S10F0.5	50.03	16.04	21.20	29.61	0.5	10
9	G10-H10F0.5	50.03	16.04	21.26	29.33	0.5	10
10	G10-S9F0.2	50.00	16.00	22.68	30.16	0.2	9
11	G10-H9F0.2	50.00	16.00	22.98	29.81	0.2	9
12	G10-S9F0.3	50.01	16.16	21.69	29.30	0.3	9
13	G10-H9F0.3	50.01	16.16	20.22	29.51	0.3	9
14	G10-S9F0.5	50.05	16.06	21.95	30.21	0.5	9
15	G10-H9F0.5	50.05	16.08	22.09	30.30	0.5	9

duration of each run was from 10 days to 7 weeks, depending on the applied load level and the waveform, and it was ensured that the test specimen was completely immersed in the seawater throughout the test period. The seawater was replaced after every 15 days in order to conform to the ASTM E647 Standard. More detail on the experimental procedure can be found elsewhere [26]. Following completion of each CF test, the crack path was investigated, and the crack length measured on the free surfaces (see Fig. 5(b & c)). Subsequently the sample was broken open, after soaking in liquid nitrogen, to measure the final crack length on the fracture surface. Fig. 5(d–h) show the nature of the fracture surface on CF test specimens (G10-H10F0.3, G10-H9F0.5G10-S9F0.3 and G10-S9F0.2 respectively), which exhibited no tunnelling and little or no difference in the crack lengths at front and back free surfaces. Fig. 5(h) is the fracture surface for the air test used in establishing calibration curves having generally no tunnelling.

3.2. Crack length estimations using back-face strain measurements

To measure the crack length in seawater tests, the back-face strain (BFS) measurement technique was employed in this study. In this technique, a strain gauge is attached to the back face on the C(T) specimen and the instantaneous crack length is empirically correlated with the amount of bending strain measured at the back of the sample under a given load level. The BFS method, which is a nonvisual technique as recommended in Ref. [53], is widely applied for crack length estimations and has been found to be more efficient and cost-effective than Alternating Current Potential Difference (ACPD), Direct Current Potential Difference (DCPD) or optical measurements for seawater tests [57]. In order to use the BFS crack length estimation technique in CF tests performed in this study, calibration curves have been derived from the air tests at different load levels. The process of deriving BFS calibration curves has been summarised in Fig. 6. Strain gauges were fitted at the back of the C(T) specimens and the microstrain readings were collected during the FCG tests using a Model P3 Strain Indicator and Recorder [58]. The optical crack lengths on the free surfaces were measured at different numbers of cycles using digital cameras. The calibration curves developed in air tests correlate the crack length, at a given number of cycles (N), with the amount of microstrain (μm) produced at the back of the sample. In the CF tests, the N vs. μm data were recorded. The calibration curves previously developed in air tests for different load levels were employed to correlate the estimated crack lengths from BFS measurements with the number of cycles. As shown in Fig. 6(b) the strain gauge on the C(T) sample in the CF tests must be isolated from the seawater by applying a suitable coating as described in Ref. [59].

Fig. 7(a) shows the calibration curves derived in air for the P_{max} loads of 12, 10 and 9 kN for the three subgrades of the S355 steels. The 9 kN calibration curve for G8 + M was extracted from Ref. [14] while the 10 kN calibration curve for G8 + M was generated in the present study as well.

The equations of the line of best fits made to the data are summarised in Table 5. As seen in Fig. 7(a), the 10 kN curve generated for NR (J2 + N) has exhibited the lowest resistance to compressive strain compared to that of G10 + M and G8 + M at the same load level. This observation is consistent with the lower yield stress value reported for NR (J2 + N) in Table 3. The calibration curves at similar load levels for the three materials examined in this study appear to suggest that the mechanical properties have an influence on the value of the microstrain in BFS calibration curves. In other words, the calibration curve varies for different steel grades and in extension the mechanical properties.

Fig. 7(b) demonstrates a comparison between the measured crack lengths with the estimated values using the BFS calibration curve equations summarised in Table 5. This figure confirms that here is an excellent correlation between the measured and calculated fatigue crack lengths within a range of 20–30 mm and this increased the confidence in the estimated crack lengths in *SW* tests.

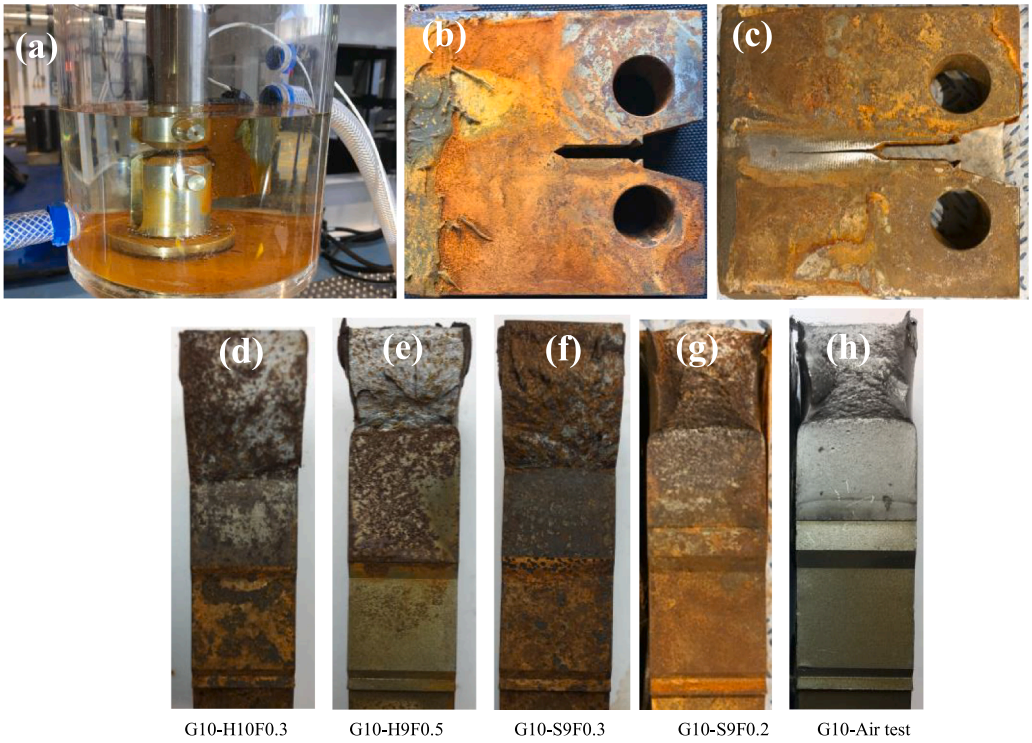

Fig. 5. (a) CF experimental set-up (b) side view of the crack path in a CF test specimen, (c & d) examples of fracture surface in two CF test specimens.

3.3. Experimental waveforms in corrosion-fatigue tests

Two waveforms have been employed in this study; *si* and trapezoid waveform with hold-time at the maximum applied load. Henceforth, the trapezoid waveform will be referred to as hold-time waveform (*h-t*). A commercial Instron software, *WaveMatrix*® [60] was used to programme the two waveforms in the CF tests. The load ratio of $R = 0.1$ was applied in all tests and the effects of different frequencies of 0.2 Hz, 0.3 Hz and 0.5 Hz on the CFCG behaviour were examined.

The loading and unloading rates for the hold-time waveform (*h-t*) were kept constant for the three frequencies and different load levels while the hold time was varied depending on the test *f*. As an example, for the 9 kN test with *h-t* the test started with 0.9 kN (i.e. P_{min}) and then the load was ramped up to 9 kN (i.e. P_{max}) at a rate of 48.6 kN/s. Upon completion of the predefined hold-time period the sample was unloaded to 0.9 kN with the same rate of 48.6 kN/s. This implies that the rise time from the P_{min} to P_{max} was about 0.17 and 0.19 s in tests with the maximum applied load of 9 and 10 kN, respectively. The frequencies 0.2, 0.3 and 0.5 Hz were generated by varying the hold time at P_{max} while the loading and unloading rates were kept at 48.6 kN/s in all the tests. Typical waveforms generated for the actual CF experiments with different waveforms and frequencies are shown in Fig. 8 for the case of 10 kN. As seen in this figure, while the loading and unloading rates were kept the same in all tests with *h-t*, the hold-time was varied depending on the applied *f* (e.g. 4.62 s and 1.62 s for the tests with applied $f = 0.2$ and 0.5 Hz respectively).

4. Evaluation of tests on FCGR

The FCGR calculation was carried out in accordance with the procedure specified in ASTM E647-15 [53] and BS EN ISO 11782-2:2008 [61]. The parameters used in seawater tests evaluation are the applied load, *P*, the crack length, *a*, the number of cycles, *N* and the microstrain (BFS), $\mu\varepsilon$. Using the appropriate calibration curve (Fig. 7 and Table 5), the με in CF tests was converted to the crack length and subsequently the SIFR was calculated. The change in the maximum stress intensity factor (SIF), K_{max}, and minimum SIF, K_{min}, in the tests was calculated using the following equation:

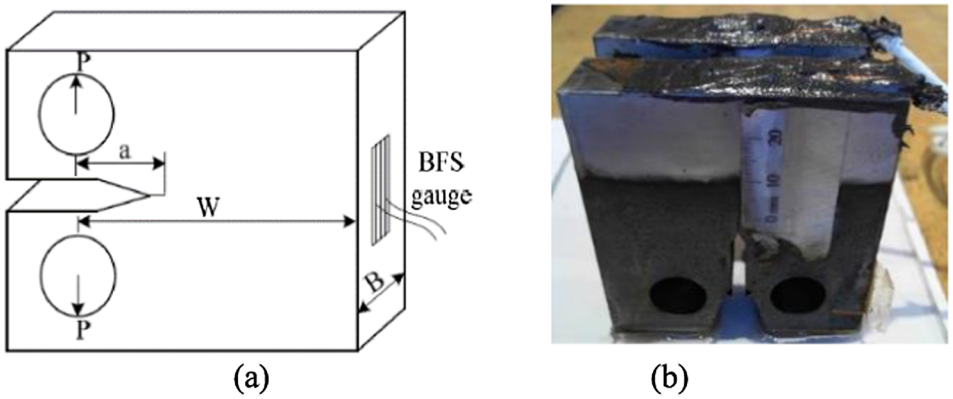

Fig. 6. (a) Schematic of a C(T) specimen with bonded strain gauge (b) strain gauge insulation during CF tests.

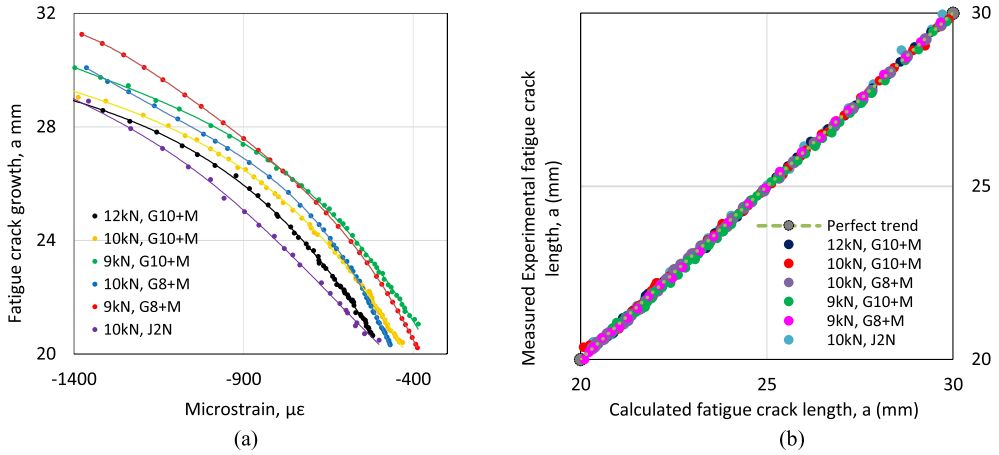

Fig. 7. (a) BFS calibration curves at different load levels (b) correlation between the measured and estimated crack lengths.

$$\Delta K = K_{max} - K_{min} = \frac{\Delta P}{B\sqrt{W}} * Y\left(\frac{a}{W}\right) \tag{1}$$

where ΔP is the difference between the maximum and minimum applied loads, W is the specimen width, B is the specimen thickness. $Y(a/W)$ is the geometry-dependent shape function, the value of which for the present C(T) specimen geometry and for $a/W \geq 0.4$ can be calculated as follows:

$$Y\left(\frac{a}{W}\right) = \frac{(2+\alpha)}{(1-\alpha)^{3/2}} * (0.886 + 4.64\alpha - 13.32\alpha^2 + 14.72\alpha^3 - 5.6\alpha^4) \tag{2}$$

where $\alpha = a/W$. A new shape function solution for C(T) specimens with a/W less than 0.4 can be found elsewhere [14]. The solutions of $Y(a/W)$ for other conventional fracture geometries can be found in fracture mechanics textbooks such as Ref. [35]. The ASTM standard suggests the use of fitted crack length, a_i, corresponding to N_i when calculating the SIFR (ΔK) associated with da/dN (see Refs. [53,61]) instead of the experimentally observed crack, a to compensate for human error in crack length measurement and material anomalies. This method tends to produce a fine correlation between da/dN and ΔK data points along the power law curve. The experimental N_i, which was read off from the computer software, was directly employed in the data analysis in the present study. Thus, the rate of crack growth, da/dN at a particular number of cycles, N_i and crack length a_i was calculated using a 7-points incremental polynomial technique following the procedure outlined in Refs. [53,61]. The value of the FCGR (i.e. da/dN) was then plotted against the corresponding ΔK on a log–log axes. The Paris law constants obtained from a straight line drawn through the linear part of the curve were derived using the following equation:

$$\frac{da}{dN} = C\Delta K^m \tag{3}$$

where C and m are the empirical power-law constants found by fitting a regression line to the test data in the Paris Region.

5. Corrosion-fatigue crack growth rate results and discussion

5.1. Test results on S355G10 + M

The CFCGR results obtained on S355G10 + M for freely corroding conditions in *SW* for the *si* and *h-t* are shown in Fig. 9. The results from these 12 tests (see Table 4) are shown in pairs in Fig. 9 in order to compare the CFCGR in S355G10 + M (denoted G10 in specimen IDs) steel subgrade for the two waveforms, under frequencies of 0.2 Hz, 0.3 Hz and 0.5 Hz. In Fig. 9(a–f) the *si* and *h-t* data points are shown with circles and triangles, respectively. Fig. 9(a–c) show the results from the tests performed at 10 kN under various frequencies while Fig. 9(d–f) present the data for 9 kN maximum applied load. It can be seen in Fig. 9(a–c) that under P_{max} = 10 kN, the *si* results have exhibited higher CFCGR in the Paris Region, compared to the *h-t* data, in all tests performed at various frequencies. Also seen is that the separation in the crack growth rates between *si* and *h-t* is more pronounced at lower frequencies of 0.2 Hz and 0.3 Hz, with the largest difference observed at 0.2 Hz. Moreover, the results show that as the *f* increases to 0.5 Hz, this separation in the CFCGRs appears to decrease and the data points from both waveforms fall upon each other below about 22 MPa√m. This reduction in the growth rate in the lower ΔK region with increase in frequency may be attributed to reduced corrosion activities at the plastic zone ahead of the crack tip. That is, less time is provided for the rate increasing corrosion reaction to take place in the plastic zone or that the size of the plastic zone is not large enough to intensify the rate increasing corrosion process. In the range of about 22–31 MPa√m, the CFCGR of the *si* is clearly higher than that of the *h-t*; similar to the results of Fig. 9(a & b). This result tends to suggest that the extent of the interaction of the damaging chemical species in the *SW* with the plastic zone fundamentally influences the CFCGR. As the driving force increases, the plastic zone size increases and the corrosion activity rises as well in the plastic zone. Because the frequency is relatively high, massive anodic dissolution of the plastic zone which may lead to crack blunting may not occur. In this instance, the CFCGR will

Table 5
Equations of the BFS calibration curves for various examined materials at different load levels.

Material	P_{max} (kN)	Calibration equations	R^2
G10	12	$a = -1.50 \times 10^{-12}(\mu\varepsilon)^4 - 1.12 \times 10^{-8}(\mu\varepsilon)^3 - 3.24 \times 10^{-5}(\mu\varepsilon)^2 - 4.48 \times 10^{-2}\mu\varepsilon + 4.72$	0.9994
G10	10	$a = -1.50 \times 10^{-12}(\mu\varepsilon)^4 - 1.10 \times 10^{-8}(\mu\varepsilon)^3 - 3.03 \times 10^{-5}(\mu\varepsilon)^2 - 4.05 \times 10^{-2}\mu\varepsilon + 7.58$	0.9995
G10	9	$a = -1.50 \times 10^{-12}(\mu\varepsilon)^4 - 1.15 \times 10^{-8}(\mu\varepsilon)^3 - 3.06 \times 10^{-5}(\mu\varepsilon)^2 - 3.89 \times 10^{-2}\mu\varepsilon + 10.0$	0.9994
G8	10	$a = -1.23 \times 10^{-11}(\mu\varepsilon)^4 - 6.08 \times 10^{-8}(\mu\varepsilon)^3 - 1.12 \times 10^{-4}(\mu\varepsilon)^2 - 9.77 \times 10^{-2}\mu\varepsilon + 6.52$	0.9998
G8	9	$a = -1.23 \times 10^{-11}(\mu\varepsilon)^4 - 5.02 \times 10^{-8}(\mu\varepsilon)^3 - 7.93 \times 10^{-5}(\mu\varepsilon)^2 - 6.60 \times 10^{-2}\mu\varepsilon + 3.90$	1.0000
J2N	10	$a = 6.42 \times 10^{-12}(\mu\varepsilon)^4 + 2.64 \times 10^{-8}(\mu\varepsilon)^3 + 3.45 \times 10^{-5}(\mu\varepsilon)^2 + 6.20 \times 10^{-3}\mu\varepsilon + 17.7$	0.9990

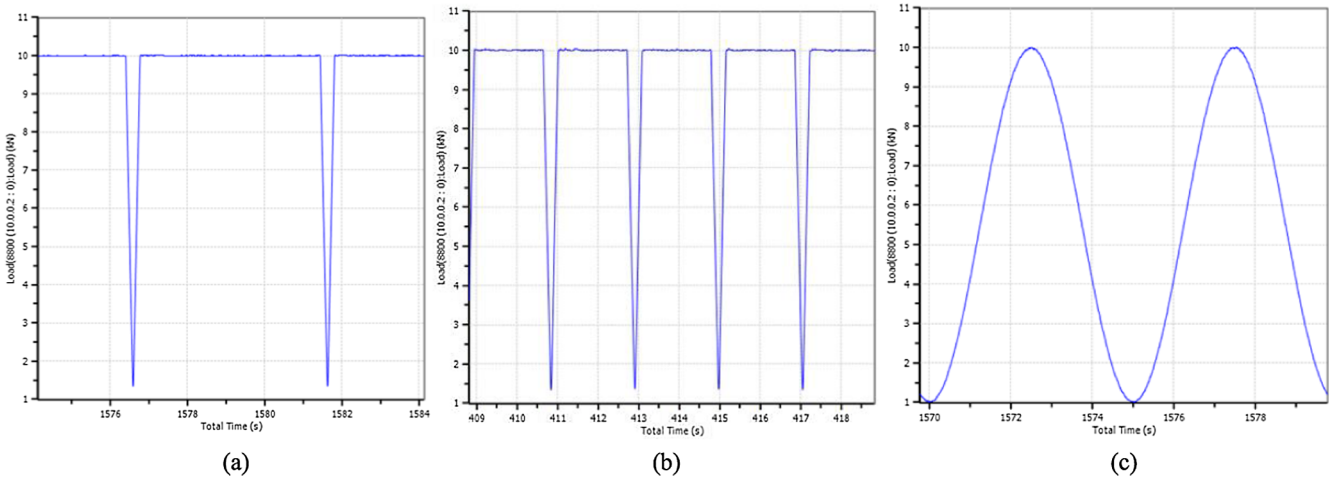

Fig. 8. Experimental waveforms for 10 kN tests (a) hold-time of 4.62 s with 0.2 Hz, (b) hold-time of 1.62 s with 0.5 Hz, (c) sinewave of 0.2 Hz.

increase. But if blunting occurs, the CFCGR may decrease and it appears that *h-t* is more susceptible to a rate retarding blunting process than *si*, especially at low frequency.

The results in Fig. 9(d–f) for the tests performed under P_{max} = 9 kN show that the difference in the crack growth rates between the two waveforms somewhat closed up in the Paris Region as compared to Fig. 9(a–c). However, the rate remained slightly higher under *si* for all the frequencies. Similar to the observed trend at the higher load level in Fig. 9(a–c), the results in Fig. 9(d–f) indicate that increasing the *f* appears to converge the CFCGRs of the two waveforms. In general, the test data presented in Fig. 9 show that for a given value of SIFR, the CFCGR is higher in *si* compared to the *h-t*. The separation between the two waveform data sets is more pronounced at the combination of lower frequencies and higher loads. This indicates that characterising the CFCG behaviour of S355G10 + M using *si* can result in more conservative life predictions for offshore structures.

In order to examine the influence of load level on the CFCGR using different waveforms, the results on S355G10 + M have been replotted in Fig. 10 for direct comparison between 9 kN and 10 kN data sets obtained using the *si* and *h-t* at various frequencies. The results in Fig. 10(a–c) show that when CF tests on S355G10 + M are performed using *si*, the change in P_{max} from 10 kN to 9 kN has little or no effect on the CFCG trends in the Paris Region for various frequencies ranging from 0.2 Hz to 0.5 Hz. However, there is a slight increase in the CFCGR for the 9 kN, 0.3 Hz test but, this trend is not obvious for the 0.2 Hz and 0.5 Hz tests. The results in Fig. 10(d–f) show that when the *h-t* is employed in CF testing noticeably higher CFCGRs are observed in 9 kN data sets, compared to 10 kN data, across the entire range of frequencies examined in this study.

As seen in Fig. 10(d–f), the influence of applied load level on the

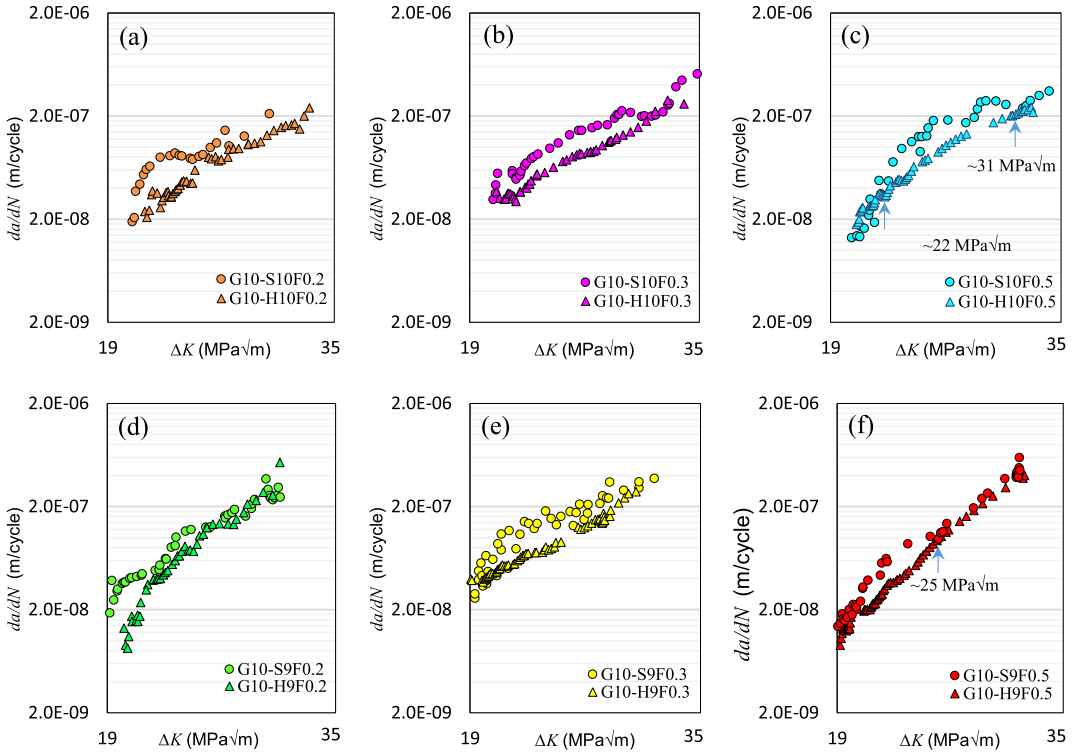

Fig. 9. The effect of waveforms on CFCGRs in S355G10 + M (a) P_{max} = 10 kN, f = 0.2 Hz, (b) P_{max} = 10 kN, f = 0.3 Hz, (c) P_{max} = 10 kN, f = 0.5 Hz, (d) P_{max} = 9 kN, f = 0.2 Hz, (e) P_{max} = 9 kN, f = 0.3 Hz, and (f) P_{max} = 9 kN, f = 0.5 Hz.

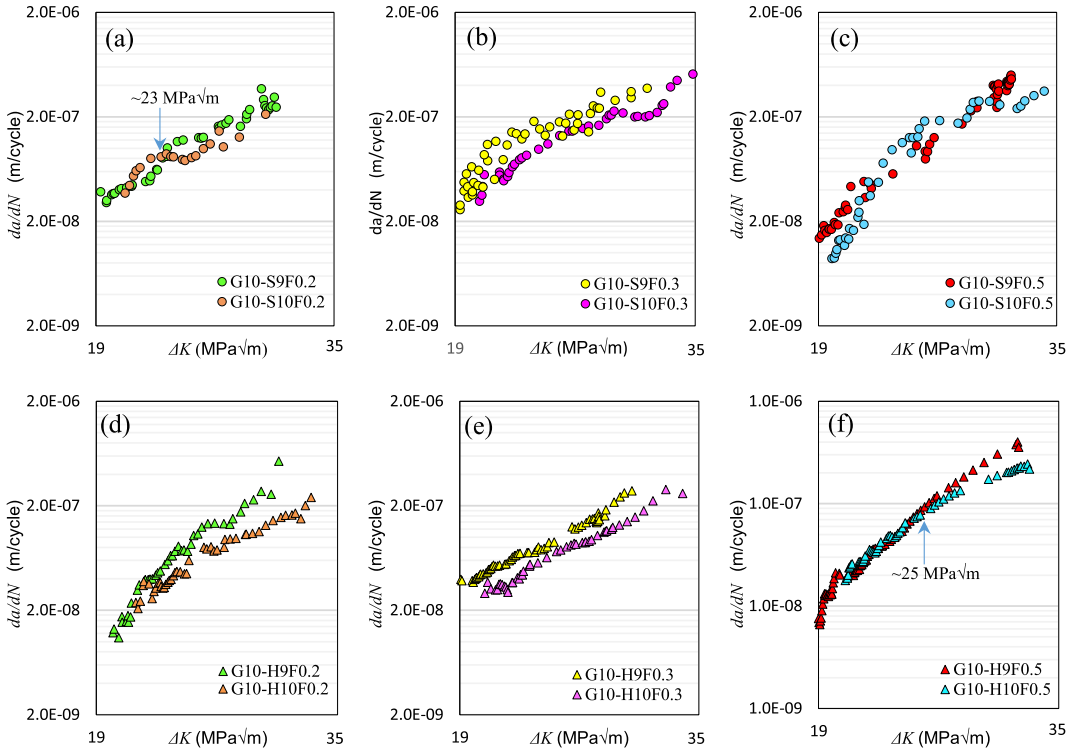

Fig. 10. The effect of load level on the CFCGR using different waveforms in S355G10 + M (a) *si* with f = 0.2 Hz, (b) *si* with f = 0.3 Hz, (c) *si* with f = 0.5 Hz, (d) *h-t* with f = 0.2 Hz, (e) *h-t* with f = 0.3 Hz, and (f) *h-t* with f = 0.5 Hz.

CFCG results obtained using *h-t* is less pronounced at the higher *f* of 0.5 Hz. In this case, the data points from 9 kN and 10 kN data sets fall upon each other at lower SIFR values. But, the curves started to diverge at higher ΔK values of about 25 MPa√m. The interesting observation is that generally, the CFCGRs at 9 kN are clearly higher than that of 10 kN data sets in Fig. 10(d–f) and fairly true in Fig. 10(a–c). This again tends to suggest that the size of the local plasticity ahead of the crack tip plays a role in decelerating or accelerating the CFCGR in seawater – since the plastic zone size depends on the fatigue load level. This effect is more visible when *h-t* is employed in the CF testing. In general, the results in Fig. 10 show that the loading effects on the CFCG behaviour of S355G10 + M tend to be more pronounced at lower frequencies and in the presence of the *h-t*.

To further investigate the effect of *f* and applied load level in the presence of different waveforms, the results obtained from all tests performed on S355G10 + M using *si* and *h-t* are collectively presented in Fig. 11(a) and Fig. 11(b) respectively. Fig. 11(a) shows that in all the CF tests performed using the *si*, within the Paris Region, there is no obvious difference in the CFCG trends for the results of the tests performed at different load levels (i.e. P_{max} of 9 kN and 10 kN) and frequencies (i.e. *f* of 0.2 Hz and 0.5 Hz). However, there is a slight increase in the CFCGR for the 9 kN, 0.3 Hz test. In other words, the sensitivity of CFCG to the *f* under *si* is small within the Paris Region, in the range of 0.2–0.5 Hz, and maximum applied load level in the range of 9–10 kN. A line of best fit has been made to the entire set of data points in Fig. 11(a) and the Paris law constants for the *si* tests are identified for $20.19 \leq \Delta K \leq 35$ MPa√m and summarized in for the G10 + M steel.

Fig. 11(b) shows that for the CF tests performed with the *h-t* there is generally no obvious trend observed in the CFCGR below a SIFR of 24 MPa√m. However, in the region with SIFR of greater than 24 MPa√m the CFCGR for 9 kN tests (with the frequencies of 0.2 Hz, 0.3 Hz and 0.5 Hz) are found to be higher than those of the 10 kN tests (with the frequencies of 0.2 Hz, 0.3 Hz and 0.5 Hz) and the results in the high SIFR region are becoming sensitive to the loading condition. This can be associated with larger plastic zones ahead of the crack tip in the higher SIFR region in the tests performed with the higher load, which has led to some level of reduction in CFCGRs. Due to the clear separation of the CFCG trends in the high SIFR region, two separate lines of best fit have been made to the 9 kN and 10 kN data points and the inferred Paris law constants are included in Fig. 11(b).

Fig. 11(c) is the comparison of the waveform tests under 9 kN. As seen previously, the CFCGR under *si* is higher under 9 kN and the rate decreased with increasing ΔK. The mean curves for the *si* and *h-t* are included. At about 28.50 MPa√m, the CFCGR of the *h-t* appears to overtake that of *si*. This tends to suggest that at very high ΔK, the CFCGR of the *h-t* will be higher. This trend can also be seen from the Paris law constants of the curves shown in the figure and listed in Tables 6 and 7. The *h-t* exponent is very high which gives the steep nature of the curve.

A similar comparison of the waveform tests under 10 kN is shown in Fig. 11(d). Under this increased load, the CFCGR of the *si* is clearly and consistently higher than that of the *h-t* in the Paris Region, though the factor of difference tends to gradually decrease with increasing ΔK. The exponential values of the Paris law, as listed in Tables 6 and 7 show also that the difference in the growth rates is gradually decreasing. Fig. 11(e) is the combination of the mean Paris curves of Fig. 11(a) and (b). Below the SIFR of about 28 MPa√m, the CFCGR under *si* is clearly higher than that of the *h-t* tests. Above this value, the CFCGR of the *si* continues to be higher than that of the 10 kN *h-t* test by an average, almost constant, factor of 1.55, but lower than that of the 9 kN *h-t* tests. The factor of difference increases with SIFR. Generally, this indicates that within the *f* range of 0.2–0.5 Hz, the life assessment of offshore wind turbine monopiles made of S355G10 + M will be more conservative when the Paris law constants from *si* CF tests are employed in the analysis.

Another important observation in Fig. 11(e) is that below about 22 MPa√m, the CFCGR of the 9 kN *h-t* is, as may be expected, lower than that of the 10 kN *h-t* test. Nevertheless, above this 22 MPa√m and at a crack growth rate of about 3.60×10^{-8} m/cycle, the 9 kN CFCGR became higher than that of the 10 kN test. Moreover, above 28 MPa√m

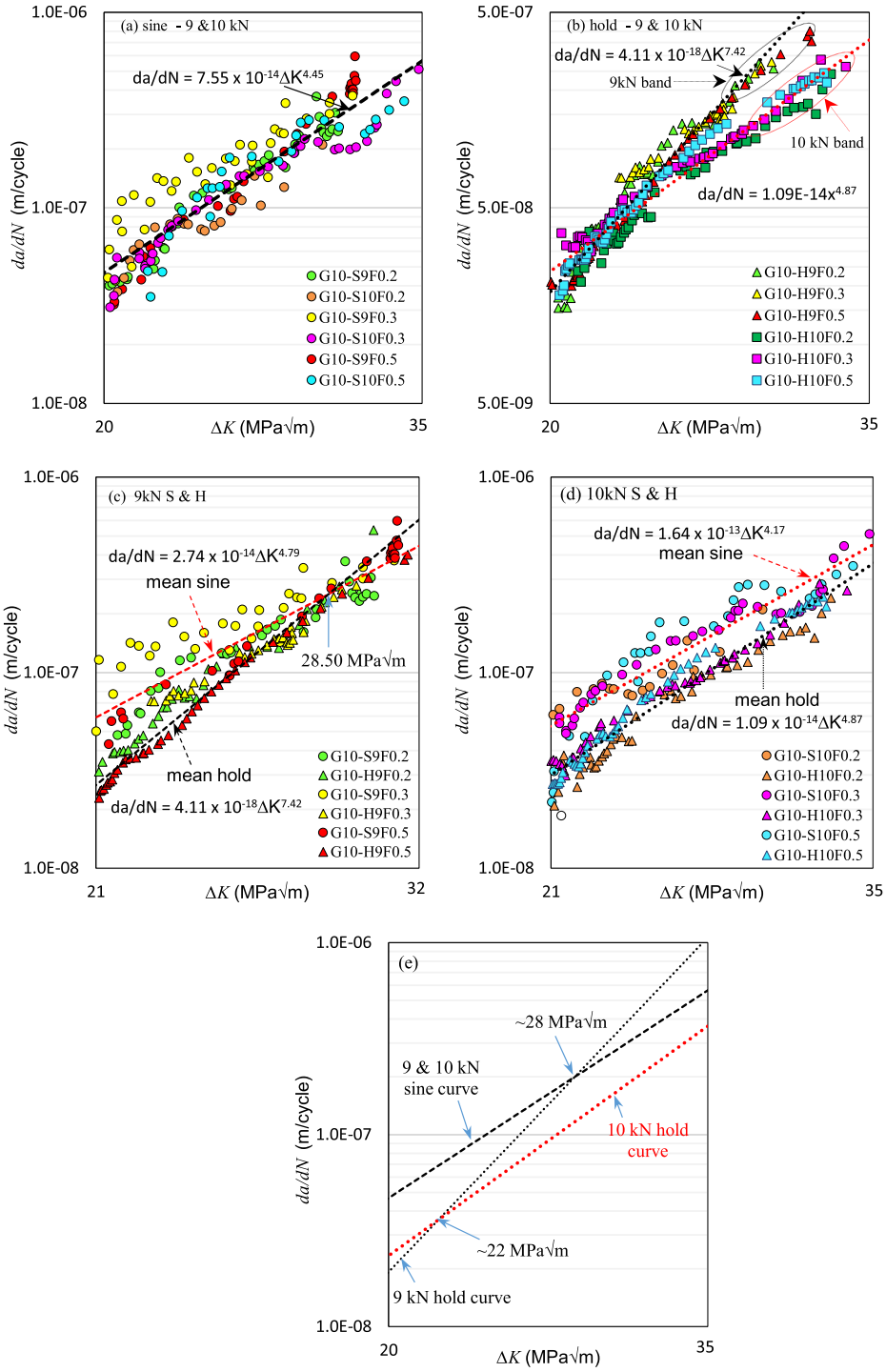

Fig. 11. The effect of waveform, frequency and load level on CFCGR in S355G10 + M under (a) *si* (b) *h-t* (c) 9 kN (d) 10 kN (e) combination of mean curves of (a) and (b).

Table 6
Paris law constants for CFCG tests performed on S355G10 + M using *si* and *h-t*.

Waveform type	Load level (kN)	*C*	*m*	R^2
si	9 & 10	7.55×10^{-14}	4.45	0.859
h-t	9	4.11×10^{-18}	7.42	0.960
	10	1.09×10^{-14}	4.87	0.965

and at a crack growth rate of about 1.42×10^{-7} m/cycle, the CFCGR of the 9 kN became even higher than even that of the *si*. This phenomenon of transitions can be explained on the basis of the plastic zone geometry (or size) interaction with the corrosion process. For the *h-t* test, below 22 MPa√m, the plastic zone size in the 10 kN is considerably smaller so that its corrosion does not lead to a rate retarding blunting process. In this domain, the higher driving force provided by the 10 kN naturally increases the CFCGR more than that of the lower driving force of 9 kN.

Table 7
Paris law constants for CFCG tests under *si* and *h-t* for all 9 kN and 10 kN data for the S355G10 + M in *SW*.

9 kN sine	C	m	R^2
Mean	2.74×10^{-14}	4.79	0.866
Mean +2SD	4.67×10^{-14}	4.79	–
Mean −2SD	1.61×10^{-14}	4.79	–
9 kN hold			
Mean	4.11×10^{-18}	7.42	0.960
Mean + 2SD	5.73×10^{-18}	7.42	–
Mean −2SD	2.95×10^{-18}	7.42	–
10 kN sine			
Mean	1.64×10^{-13}	4.17	0.912
Mean + 2SD	2.46×10^{-13}	4.17	–
Mean −2SD	1.10×10^{-13}	4.17	–
10 kN hold			
Mean	1.09×10^{-14}	4.87	0.965
Mean + 2SD	1.41×10^{-14}	4.87	–
Mean −2SD	8.41×10^{-15}	4.87	–

As the SIFR increases, the plastic zone size gradually becomes larger and the rate retarding blunting process becomes significant. In this domain, the blunting of the main active crack tip due to an increase in the plastic zone size becomes the CFCGR controlling factor rather than the load level for the *h-t*. The same can be said of the *si*, but the effect of the plastic zone size blunting process appears to be less severe up to about SIFR of 28 MPa√m than that of the *h-t*. At high SIFR, the blunting process in the *si* became significant to the point that its CFCGR became lower than that of the 9 kN *h-t* test. This transition at 28 MPa√m, appears to support the assertion that the main crack tip blunting process is the primary factor controlling the CFCGR of steel at high SIFR and low *f* in seawater. This study also found that varying the *f* in the range 0.2–0.5 Hz has little or no effect on the CFGCR process.

5.2. Test results on S355G8 + M and S355J2 + N

To verify the trends observed in Figs. 9, 10 and 11 for the S355G10 + M steel, one additional test on S355G8 + M (denoted G8-H10F0.2 in Table 4) and two additional tests on S355J2 + N (denoted J2N-S10F0.2 and J2N-H10F0.2 in Table 4) were conducted under P_{max} = 10 kN, f = 0.2 Hz and R = 0.1. The results from these tests are presented in Fig. 12(a) and (b) for S355G8 + M and S355J2 + N respectively, along with the CFCGR test data from previous studies on the same batches of material conducted using *si* by Mehmanparast [14] (denoted G8-S9F0.3A3, G8-S9F0.3A4, G8-S10F0.3B3 and G8-S10F0.3B4) and Adedipe [62] (denoted J2N-S9F0.4, J2N-S9F0.3 and J2N-S12F0.3). It can be seen in Fig. 12(a) that the CFCGR in the test with the *h-t* is generally lower than those obtained from *si* tests, This observation confirms that similar to S355G10 + M steel, the CFCG behaviour of S355G8 + M is sensitive to the cyclic waveform and lower trends are obtained when the tests are performed with *h-t*. It is also becoming evident from Fig. 12(a) that similarly to S355G10 + M, the tests with *si* on S355G8 + M exhibited no sensitivity to the maximum applied load level, in the range of 9–10 kN and within the Paris Region.

The results in Fig. 12(b) show similar results to the case of S355G10 + M and S355G8 + M. The *h-t* reduced CFCGRs for S355J2 + N compared to the results obtained from *si* tests. It can be seen in this figure that for test under P_{max} = 10 kN and f = 0.2 Hz, a lower CFCG trend is obtained from the *h-t* test compared to the *si*, and the separation between the two data sets increased for higher SIFR. As seen in Fig. 12(b), under the same loading condition the CFCGR in the *h-t* test for S355J2 + N can be up to three times lower than the *si* test. Also seen in Fig. 12(b) is that for the *si* tests, increasing the load level has some accelerating effect on the CFCG behaviour of S355J2 + N in the high SIFR region. Another important observation is that increasing the load level and decreasing the *f* (e.g. for say J2N-S10F0.2, PS) had a crack growth retarding effect in *SW* – as compared for example with the J2N-S9F0.3, PS curve. This is probably because the larger plastic zone created by the high driving force and more time allowed for the corrosion process to attack the plastically deformed region by frequency reduction may have resulted in severe crack tip blunting. Finally, it can be seen in this figure that P_{max} (in the range of 9–10 kN) is found to have a more profound influence on CFCGR than the cyclic *f* (in the range of 0.2–0.4 Hz).

5.3. Comparison of the corrosion-fatigue crack growth behaviour in NR and TMCP steels

The results from all the CF tests, which were performed in this study on S355G10 + M, S355G8 + M and S355J2 + N steels using *h-t* cycles are collectively presented in Fig. 13 and compared to each other. As seen in this figure, under the same loading conditions (i.e. P_{max} = 10 kN and f = 0.2 Hz) the CFCG trend in S355J2 + N is generally much higher than those obtained for S355G10 + M and S355G8 + M. However, the trends cross over each other in the high SIFR region due to the lower slope observed in the S355J2 + N data set. It is also obvious that although similar trends have been observed in S355G10 + M and S355G8 + M tests under similar loading conditions, the CFCGR in

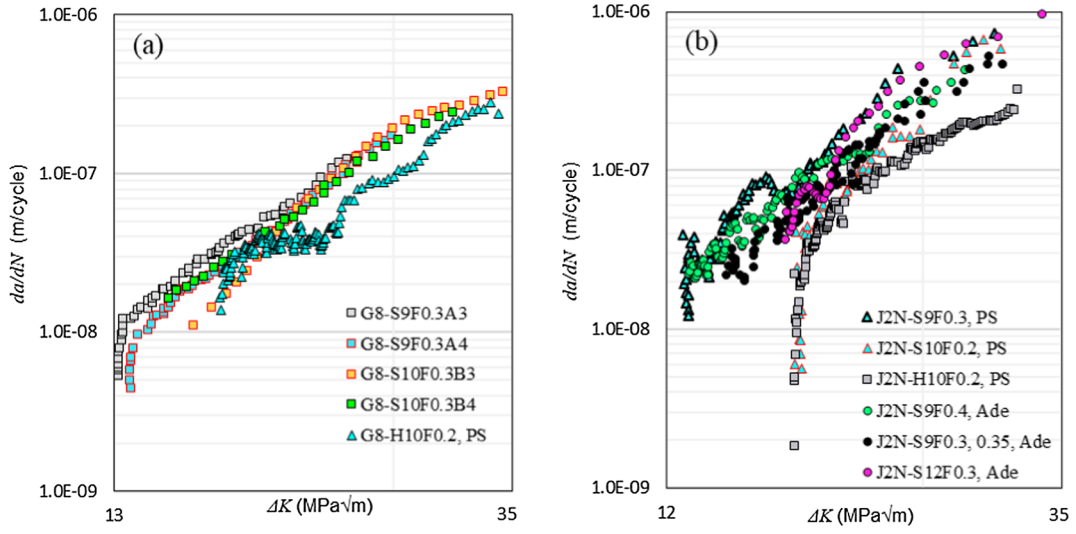

Fig. 12. Comparison of new test results on (a) S355G8 + M and (b) S355J2 + N, with the literature data. (PS – present study, Ade – Adedipe).

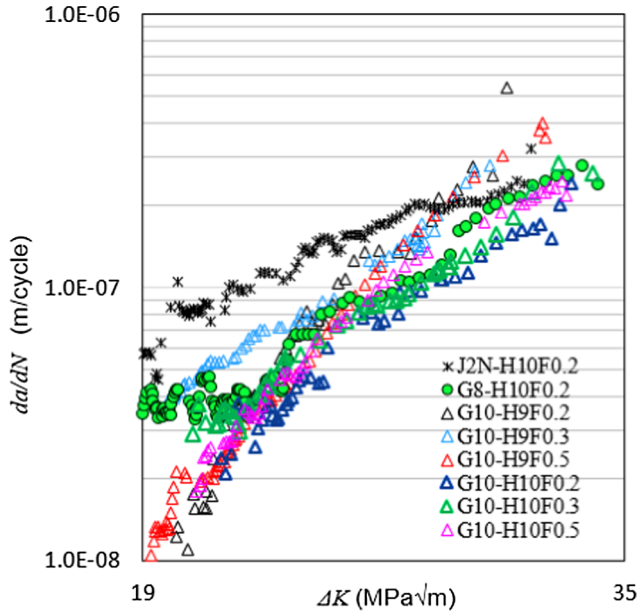

Fig. 13. Comparison of CFCG results for S355G10 + M, S355G8 + M and S355J2 + N steels under h-t.

S355G8 + M could be up to twice higher compared to S355G10 + M. This indicates that the generalisation of the CFCG behaviour in all the ferritic steels is invalid and each grade of NR or TMCP steel must be characterised separately.

Fig. 14 presents the plot of the CFCG data for all the ferritic steels obtained under *si* only at different frequencies within the range 0.05 Hz to 0.5 Hz. This figure includes all the test results obtained from *si* CF tests conducted in the present study as well as the literature data on other ferritic steels, the details of which can be found in Table 8. The tests on S355J2 + N steel are represented with triangles and coloured yellow and the replotted data of CFCGR of NR steels from the literature is represented with squares and coloured turquoise. The CFCGR data for the TMCP steels is represented with circles and coloured red. The general observation from the comparison of such a wide range of ferritic steels tested under different loading conditions suggests that the plot, irrespective of the frequency range (0.05–0.5 Hz) and stress ratio in the range of 0.0–0.67, the CFCGRs can be separated into two domains; the upper domain for the normalised steel and the lower domain for the TMCP steels. This separation is proposed to be a consequence of the microstructural features, as we will see later in Section 6.

In Fig. 14, bi-linear CFCG trends can be observed for the normalised steels (NR), which is similar to the 2-stage recommendations made in BS7910 Standard [55]. Two-stage (A and B) lines – the solid black line is the mean value and the dash black line the mean + 2SD curve, are shown in Fig. 14. The mean solid line appears to denote the possible boundary (diffused) between the data cloud for the NR and TMCP steels in the range 13.33–50 MPa√m as all the data points of the TMCP are below this line. The Stage A mean curve of the NR steel is described by the Paris equation $1.24 \times 10^{-13}\Delta K^{4.60}$ while that of its B is described by $2.70 \times 10^{-9}\Delta K^{1.64}$. The Stage A mean + 2SD curve for the NR steels is described by the Paris law $2.28 \times 10^{-13}\Delta K^{4.60}$ while the Stage B is described by $4.28 \times 10^{-9}\Delta K^{1.67}$. The Paris law constants are also presented in Table 9. It can be seen in Fig. 14 that within the wide range of load levels and frequencies considered in these studies, the CFCGR is generally found to be lowest in S355G10 + M TMCP steel, followed very closely by S355G8 + M TMCP steel used in the SLIC study [14] and lastly the NR steels.

The results presented in Fig. 14 suggest that the level of scatter in normalised steels can be higher than TMCP steels, though more tests on a wider range of subgrades of TMCP steels must be performed to confirm this observation. The Re-squared value for the Stage B curve shows considerable scatter. This level of scatter is expected at high ΔK or when the crack growth has entered the failure stage, where microvoid

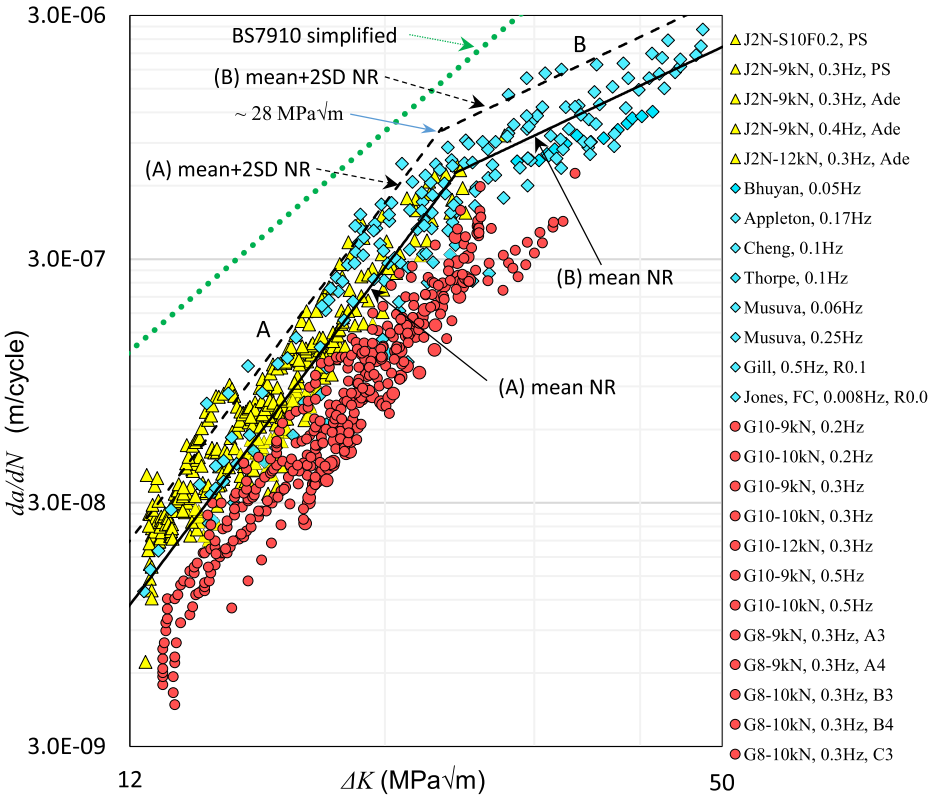

Fig. 14. Comparison of the CFCG data for all the ferrite-pearlite steels considered in this study under *si*.

Table 8
Paris Loading conditions for the CFCG tests conducted by other researchers.

Study by	Steel grade	Wave form	Env.	*f* (Hz)	*R*
Bhuyan [44]	CSA G40.21 M 350	*si*	*SW*	0.05	0.1
		p-s	*SW*	0.1	0.1
Scott [11]	BS4360-50D	*p-s*	*SW*	0.2	0.5
		t	*SW*	0.1	0.5
		n-s	*SW*	0.2	0.5
Appleton [46]	BS4360-50D	*si*	*SW*	0.17	0.5
		t	*SW*	0.17	0.5
Cheng [13]	ABS grade EH36	*si*	*SW*	0.1	0.1
Dhinakaran [63]	C-Mn steel	*si*	NaCl	1.0	0.5
Thorpe [5]	BS4360-50D	*si*	*SW*	0.1	0.0, 0.1
Adedipe [57]	S355J2N	*si*	*SW*	0.3, 0.35, 0.4	0.1
Musuva [30]	BS4360-50D	*si*	3.5%NaCl	0.25	0.08
		si	3.5%NaCl	0.06	0.08
Gill [64]	HSLA (MF-80)	*si*	3.5%NaCl	0.5	0.67
		si	3.5%NaCl	0.5	0.1
Barsom [27]		*si* & *tr*	NaCl	0.1	0.1
Present Study and Mehmanparast [14]	S355G8 + M	*si*	*SW*	0.3	0.1
Present Study	S355G10 + M	*si*	*SW*	0.2, 0.3, 0.5	0.1
Present Study	S355J2N	*si*	*SW*	0.2, 0.3	0.1

si = sine, *tr* = triangular, *p-s* = positive sawtooth, *n-s* = negative sawtooth, *SW* = seawater.

Table 9
Two-stage Paris law constants for NR data cloud in Fig. 14.

Material	C (Stage A)	m (Stage A)	R^2	C (Stage B)	m (Stage B)	R^2	ΔK transition from A to B
Mean NR	1.24×10^{-13}	4.60	0.8838	2.70×10^{-9}	1.64	0.5987	~29.0
Mean + 2SD - NR	2.28×10^{-13}	4.60	–	4.28×10^{-9}	1.64	–	~28.0

coalescence mechanism dominates., this scatter appears to be a function of the morphologies of the microconstituents of the steel which influenced the extent of the crack bifurcation, diversion and crumb formation found during metallographic study of the crack path in the present study (see Section 6). The green dotted line is the simplified BS7910 recommendation curve which still provides a satisfactory design estimate of the FCG behaviour for these grades of steel in *SW*. Nonetheless, it is over-conservative for the TMCP steels. Finally, with regard to the whole data, this figure shows that the difference between the CFCGRs at the lower bound and upper bound data can be up to around an order of magnitude. This suggests that the CF behaviour of each subgrade of NR and TMCP steels must be carefully characterized for a given loading condition and the CFCG behaviour in the entire range of ferritic steels cannot be defined using a single trend.

6. Metallography and fractography analyses

6.1. Analysis of untested samples

To understand the disparity in the CFCGR between the waveforms under the test conditions discussed above, a metallographic study was carried out. The first step was to determine the phases present in these steel subgrades. This involved the use of optical and scanning electron microscopy (SEM) techniques. The microstructures of the three S355 steel subgrades examined in this study are shown in Fig. 15. In Fig. 15(a–c) the optical micrographs with magnification scale of 20 μm are presented while Fig. 15(d–f) are the corresponding SEM micrographs obtained at 50 μm. Fig. 15(g & h) were obtained at 2 μm while Fig. 15(i) was at 10 μm. As seen in Fig. 15, the S355 steel subgrades examined in this study have microstructures consisting essentially of a ferrite (α) matrix with varying volume fractions of pearlite (*P*). The microstructures of S355G10 + M and S355G8 + M are almost similar to each other, but different from S355J2 + N.

Three types of ferrite were observed with the aid of Energy-dispersive X-ray Spectroscopy (EDX) compositional analysis, as noted in Fig. 15(g–i). For clarity, these will be referred to as high relief ferrite (α_{HR}) indicated by the red[1] arrows, low relief ferrite (α_{LR}) indicated by the green arrows and high alloy ferrite (α_{HA}) denoted by blue arrows. Note that the difference in carbon content between the α_{HR} and α_{LR} is relatively small, if not negligible. The pearlite (*P*) in Fig. 15 is indicated by black arrows. The high alloy ferrite (α_{HA}) phase formed from the austenite as a thin ribbon completely covering the α_{LR} grain surfaces. It is concluded from the EDX analysis that this thin ferrite ribbon actually has carbon content approaching that of *P* with segregation of allowing elements such as Al, Mg, Si and 'impurities' such as O, S and P. The detailed analysis of the alloying constituents of this phase is ongoing. Note that the low and high relief α phases could not be distinguished under optical micrographs.

Moreover, sub-grains are seen in the α_{LR} ferrite phase as shown by the smaller yellow arrows in Fig. 15(g & i). The formation of these sub-grains may be due to heating and re-heating processes inherent in the TMCP steel production technique [65]. With prolonged heating, carbon and other alloying elements may have diffused further producing these sub-grains which appear to be surrounded by the α_{HA} phase along the sub-grain surfaces. The *P* colonies in the TMCP steels are somewhat slender and elongated. In the TMCP steels, the *P* appears to grow in two forms – small-blocky colonies and the thin, elongated or needle-like morphology colony that perhaps developed from the α_{HA} phase. In the S355J2 + N steel the *P* colonies are large, blocky and dense as can be seen in Fig. 15(f & i). Clearly, the phase morphologies in the S355J2 + N and S355G8 + M/G10 + M TMCP steels are different. Therefore, dissimilar local microstructural properties and corrosion process variation are expected. The presence of a hard phase (*P*) in a soft matrix (α) with dissimilar stiffnesses is expected to influence local fatigue behaviour of the steel [66] and may influence the way waveform affects the CFCGR.

[1] For interpretation of colour in Figs. 15 and 17, the reader is referred to the web version of this article.

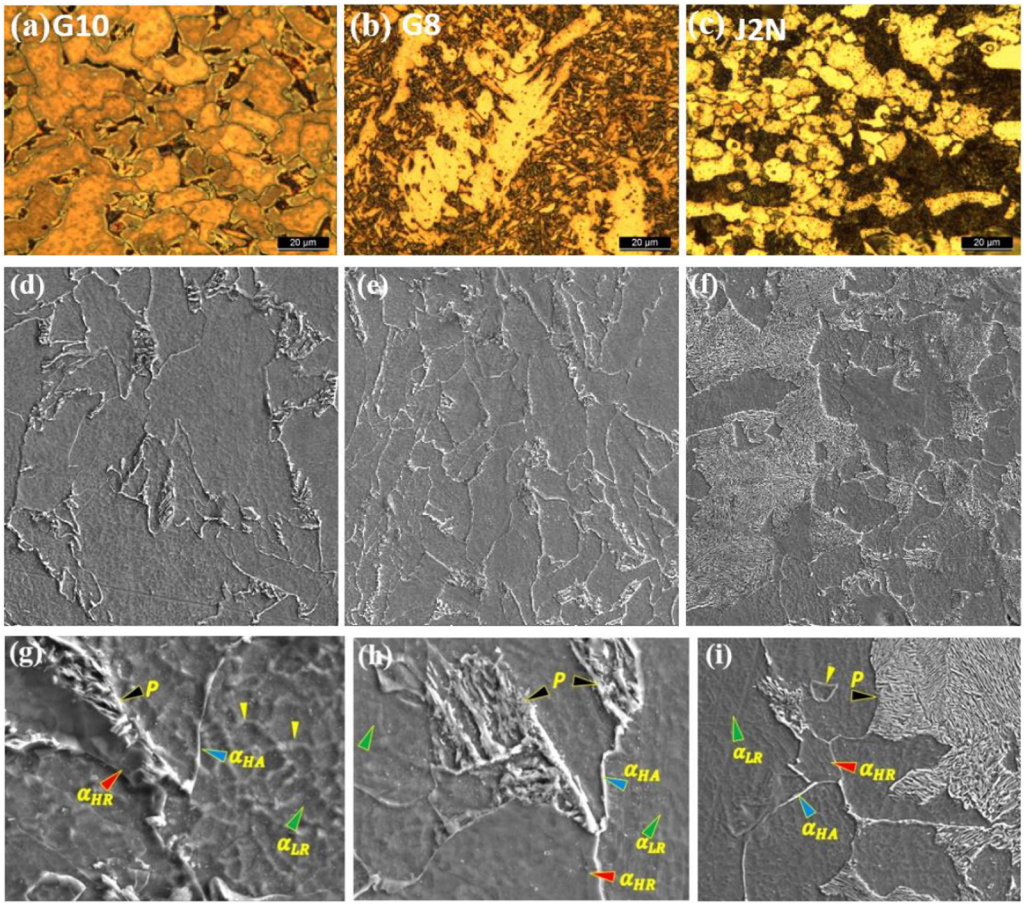

Fig. 15. The optical and SEM micrographs of the S355 steel samples examined in this study (a, d, g) S355G10 + M (b, e, h) S355G8 + M (c, f, i) S355J2 + N.

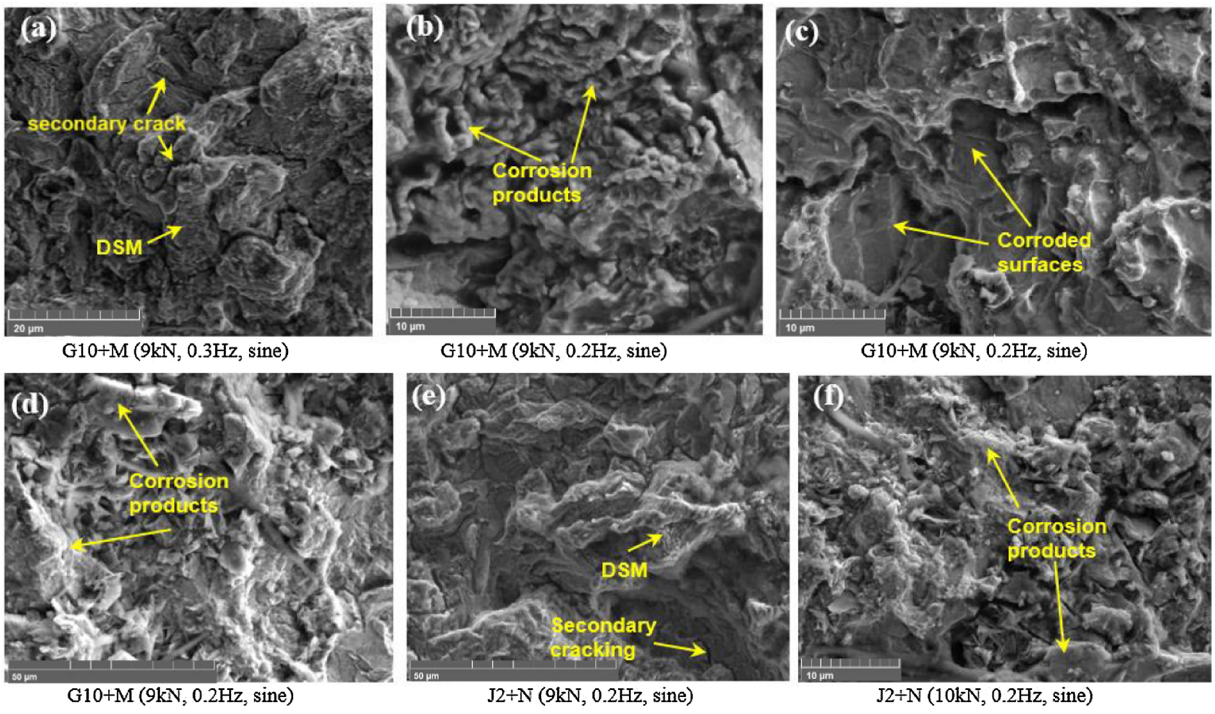

Fig. 16. Fractographs of fracture surfaces of corrosion-fatigue testes specimens (a–d) for S355G10 + M, (e & f) for S355J2 + N.

6.2. Post-mortem analysis of corrosion-fatigue tested specimens

Some examples of the post-mortem analysis on CF tested samples for S355G10 + M and S355J2 + N are shown in Fig. 16. Post-failure examination of the fracture surface of CF specimens shows that the striations in the samples tested in *SW* appeared to be washed out by the corrosion process. This washing out process progressed with time for the S355G10 + M steel as can be seen in Fig. 16(a)–(d). Fig. 16(e & f) show the fracture surface of S355J2 + N samples in *SW* and the characteristics are similar to that observed in the TMCP steels (i.e. S355G10 + M). Generally, cleavage failure was not observed in seawater tests. The ductile striation mechanism (DSM) as seen in the fractograph (see Fig. 16(a & e)) is typical of the failure mechanism towards the end of the Paris Region for low carbon steel. These fractographs do not give any clue as to the difference in CFCGRs observed for the two waveforms under the test conditions discussed previously. An alternative approach is to examine the crack path and the features influencing crack growth in the materials.

6.3. Crack path analysis on corrosion-fatigue tests specimens

The crack path study was carried out on a G10-S10F0.5 specimen, which was tested using *si*, and the results are presented in Fig. 17. This test was performed on a S355G10 + M specimen with P_{max} = 10 kN and f = 0.5 Hz. The direction of the crack growth in this study was from left to right and the direction of the applied fatigue force was normal to the crack path (as shown by a yellow double-sided arrow). High angle diversion (as noted by the red arrows), branched crack front (indicated by black arrows) and formation of metal crumbs (indicated by white arrows) occurred, as shown in Fig. 17. Note that there were very few high angle crack tip diversions and branching compared to the observations made in the air tests on the same material (not presented here). Formation of metal crumbs was less in the G10-S10F0.5 specimen than in air, in the range of approximately 18–22 MPa√m. There was also the widening of the gap between the fatigued surfaces in comparison with air tests, an effect attributed to corrosion. The branched crack tips maintained some sharpness. The magnified micrographs on the right of Fig. 17 show branched crack tips with some degree of tip blunting. This is more considerable at locations 5, 6 and 7 identifying features, which occurred at high SIFR. Locations 2 and 5, feature severe blunting to the extent that another crack front budded or nucleated from its side. This suggests that increasing the fatigue load to a level where the crack opening displacement is significant in *SW* can result in some degree of crack tip blunting which may retard the crack growth. This blunting is a consequence of anodic dissolution of the plastically deformed region ahead of the crack tip. Increasing the fatigue load (or SIFR) or the hold-time at the P_{max} permits more damaging species to penetrate the plastic zone which may lead to rapid dissolution reaction and consequently crack growth retardation in a severe case.

A crack path analysis was also carried out on a G10-H10F0.2 specimen, which was tested using *h-t*. The results are presented in Fig. 18. This test was performed on a S355G10 + M specimen with P_{max} = 10 kN and f = 0.2 Hz. The direction of the crack growth in this study was from left to right and the direction of the applied fatigue force was normal to the crack path (yellow arrows). Initially, a low angle crack diversion and branching similar to that seen in Fig. 17 was observed. Similar features of high angle diversion (as noted by the red arrows), branched crack front (indicated by blue arrows) and formation of metal crumbs (indicated by white arrows) occurred on this specimen. The basic difference between this specimen, which was tested with *h-t*, and the test conducted under *si* is that the branched crack tips are extensively blunted as shown on the top right of Fig. 18. Locations 1–7 features clearly show the severe blunting that occurred at the lower SIFR under 10 kN in the low f test (f = 0.2 Hz) performed with *h-t*. The yellow boxes (features 8–15) show that the severe blunting process occurred also at the high SIFR in this specimen. The point of test stoppage is encircled (location 16) and it can be seen that the tip of the main propagating crack front is considerably blunted as shown by the magnified micrograph on the bottom right. As mentioned previously, this varying amount of crack tip blunting can be associated with the anodic dissolution of the local plasticity ahead of the crack tip. The severity of the blunting appears to increase with an increase in the size of the local plastic region. Note that the plastic zone size is a function of the magnitude of the SIFR or the driving force. Large plastic zone size could lead to faster transportation of more damaging chemical species through the crack tip into the deformed region due to an increase in the crack opening displacement. Blunting in the hold-time is found to be more severe due to the longer hold-time for corrosion attack. This possibly explains why lower CFCG trends were observed in all the samples tested using *h-t* as compared to *si* (see Figs. 9, 11(c & d) and 12).

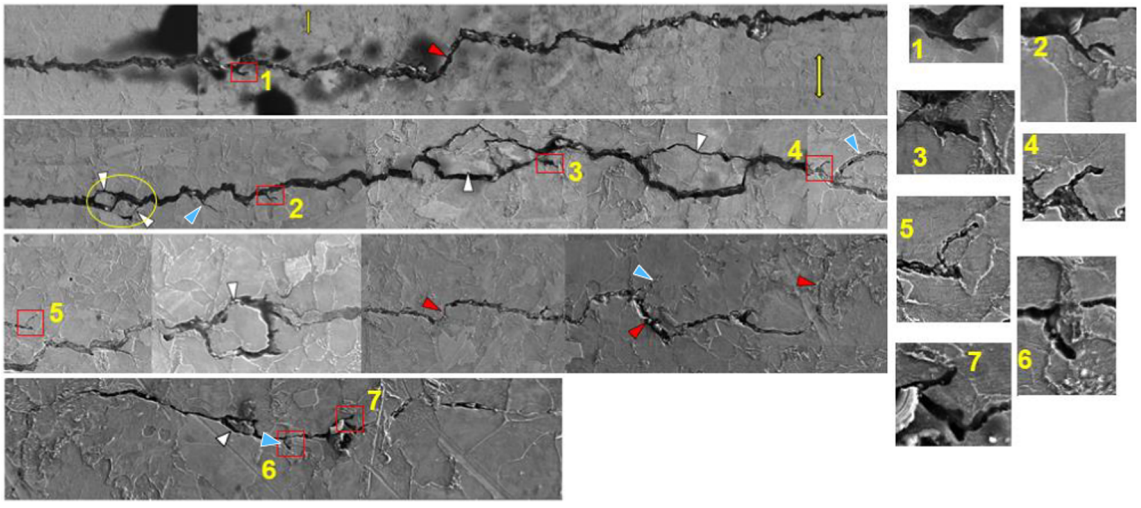

Fig. 17. Crack path analysis on G10-S10F0.5.

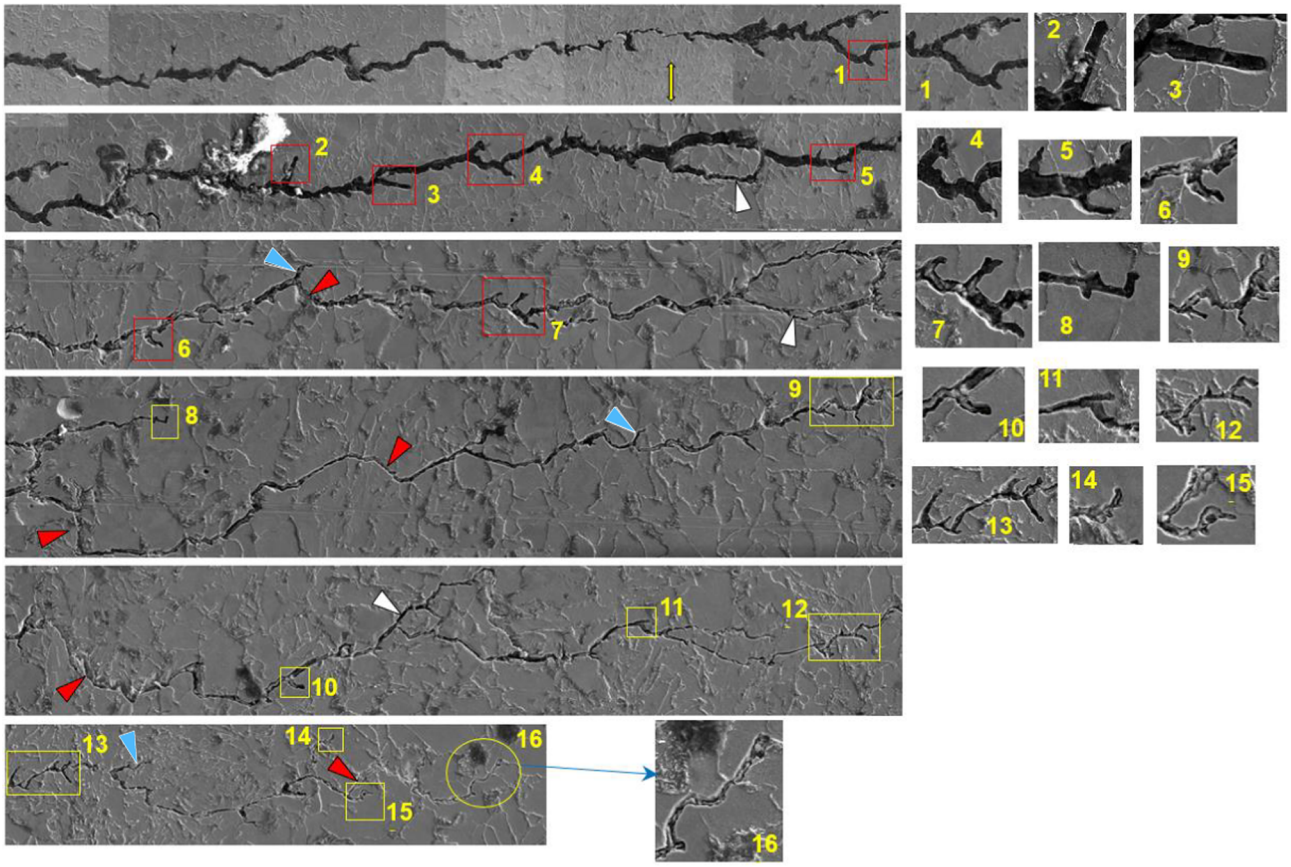

Fig. 18. Crack path analysis on G10-H10F0.2.

7. Conclusions

The current study investigated the sensitivity of the CFCGR of the S355 steel subgrades S355G8 + M, S355G10 + M and S355J2 + N to waveform, f and load level in *SW*. The waveforms considered in this study are sinewave (*si)* and trapezoid waveform (generally referred to here as hold-time (*h-t)*) and the experiments were conducted under frequencies of 0.2 Hz, 0.3 Hz, 0.5 Hz. The stress ratio in all tests was 0.1 and the maximum applied loads were 9 kN and 10 kN. Results regarding S355G10 + M have shown that the CFCGRs are higher in *si* tests compared to the *h-t* and this effect is more pronounced at lower frequencies (i.e. f = 0.2 Hz) and higher applied loads (i.e. P_{max} = 10 kN). Moreover, it has been shown that in the tests performed using *h-t*, the CFCGR in the Paris Region increases slightly with a decrease in the load level, while little or no noticeable difference was observed during the *si* tests with different load levels. The results from additional tests on S355G8 + M and S355J2 + N have shown that these two subgrades of S355 are also sensitive to the cyclic waveform and up to three times lower CFCG trends can be obtained when the tests are performed with *h-t*. Comparison of the experimental results on S355G8 + M, S355G10 + M and S355J2 + N has shown that under both *si* and *h-t*, the CFCG trend in normalised steels (e.g. S355J2 + N) is higher than TMCP steels (e.g. S355G8 + M, S355G10 + M). Post-mortem analysis on the fracture surface of CF specimens has shown that the CFCG mechanism is by striations which appeared to be washed out by the corrosion process. It was also observed in the metallurgical analysis of the crack paths that for tests under the same load level (i.e. P_{max} = 10 kN), the specimen tested with *h-t* has exhibited extensively blunted branched crack tips. This explains why the CFCG trends are lower in *h-t* tests compared to *si*. It is found that the main crack tip blunting process appears to be the primary factor controlling the CFCGR of steel at high SIFR and low f in seawater. Other fundamental factors controlling the CFCGR of steel are crack angle diversion, branching of crack front and formation of metal crumbs along the crack path. The results from this study show that the use of *si* Paris law constants for structural integrity assessment will be a conservative approach for OWT monopile foundations.

Declaration of Competing Interest

The authors declare that they have no known competing financial interests or personal relationships that could have appeared to influence the work reported in this paper.

Acknowledgements

This work was supported by grant EP/L016303/1 for Cranfield, Oxford and Strathclyde Universities' Centre for Doctoral Training in Renewable Energy Marine Structures - REMS (http://www.rems-cdt.ac.uk/) from the UK Engineering and Physical Sciences Research Council (EPSRC).

Appendix A. Supplementary material

Supplementary data to this article can be found online at https://doi.org/10.1016/j.ijfatigue.2020.105484.

References

[1] Jaske CE, Payer JH. Balint VS. Corrosion fatigue of metals in marine environments. MCIC Report. 1981; (July).
[2] Pao P. Mechanisms of corrosion fatigue. ASM Handbook Volume 19, Fatigue and

Fracture (ASM International). 1996; 19: 8. Available at: www.asminternational.org.
[3] Lee SJ, Han MS, Jeong JY, Kim MJ, Kim SJ. Time and temperature dependent damage characteristics of 5083 Al alloy under cavitation-corrosion condition. Acta Phys Pol A 2016;129(4):747–52. https://doi.org/10.12693/APhysPolA.129.747.
[4] Gallagher JP. Corrosion Fatigue Crack Growth Behavior Above and Below K-Iscc. 1970. Available at: http://www.dtic.mil/dtic/tr/fulltext/u2/708377.pdf (Accessed: 31 July 2018).
[5] Thorpe TW, Scott PM, Rance A, Silvester D. Corrosion fatigue of BS4360:50D structural-steel in seawater. Int J Fatigue 1983;5(3):123–33.
[6] Knop M, Heath J, Sterjovski Z, Lynch SP. Effects of cycle frequency on corrosion-fatigue crack growth in cathodically protected high-strength steels. Procedia Eng 2010;2(1):1243–52. https://doi.org/10.1016/j.proeng.2010.03.135.
[7] Khan M, Burch I. Effect of seawater on the fatigue life and crack growth behaviour of a new microalloyed steel for submarine hull application. Int J Fatigue 1992;14(5):313–8. https://doi.org/10.1016/0142-1123(92)90482-R.
[8] Jones BF. The influence of heat treatment on low frequency fatigue crack grow th rates for a marine steel tested in air and seawater. Int J Fatigue 1981(October):167–72.
[9] Gooch TG, Booth GS. Corrosion fatigue of offshore structures. Metal Sci 1979;13(7):402–10. https://doi.org/10.1179/msc.1979.13.7.402.
[10] Nakasa K, Takei H. Mechanism of corrosion fatigue crack propagation in high strength steels. Eng Fract Mech 1983;17(5):449–59.
[11] Scott PM, Thorpe TW, Silvester DRV. Rate-determining processes for corrosion fatigue crack growth in ferritic steels in seawater. Corros Sci 1983;23(6):559–75.
[12] Jones BF. The influence of heat treatment on low frequency fatigue crack growth rates for a marine steel tested in air and seawater. 1981; (October): 167–72.
[13] Cheng Y. The fatigue crack growth of a ship steel in seawater under spectrum loading. Int J Fatigue 1985;7(2):95–100. https://doi.org/10.1016/0142-1123(85)90039-8.
[14] Mehmanparast Ali, Brennan Feargal, Tavares Isaac. Fatigue crack growth rates for offshore wind monopile weldments in air and seawater: SLIC inter-laboratory test results. Mater Des 2017;114:494–504. https://doi.org/10.1016/j.matdes.2016.10.070.
[15] Igwemezie Victor, Mehmanparast Ali, Kolios Athanasios. Current trend in offshore wind energy sector and material requirements for fatigue resistance improvement in large wind turbine support structures – A review. Renew Sustain Energy Rev 2019;101:181–96. https://doi.org/10.1016/j.rser.2018.11.002.
[16] Brennan FP. A framework for variable amplitude corrosion fatigue materials tests for offshore wind steel support structures. Fatigue Fract Eng Mater Struct 2014;37(7):717–21. https://doi.org/10.1111/ffe.12184.
[17] Bhattacharya S, Nikitas N, Garnsey J, Alexander NA, Cox J, Lombardi D, Muir Wood D, Nash DFT. Observed dynamic soil–structure interaction in scale testing of offshore wind turbine foundations. Soil Dyn Earthquake Eng 2013;54:47–60. https://doi.org/10.1016/j.soildyn.2013.07.012.
[18] Lombardi Domenico, Bhattacharya Subhamoy, Muir Wood David. Dynamic soil—structure interaction of monopile supported wind turbines in cohesive soil. Soil Dyn Earthquake Eng 2013;49:165–80. https://doi.org/10.1016/j.soildyn.2013.01.015.
[19] Henderson AR. Design Methods for Offshore Wind Turbines at Exposed Sites (OWTES): Hydrodynamic Loading on Offshore Wind Turbines; 2003.
[20] DNV/Risø. Guidelines for design of wind turbines. Det Norske Veritas: Wind Energy Department. 2002. Available at: DOI: ISBN 87-550-2870-5 (Accessed: 5 April 2016).
[21] University of Strathclyde. The Practicality and Challenges of Using XL Monopiles for Offshore Wind Turbine Substructures - Cost Analysis. 2015. Available at: http://www.esru.strath.ac.uk/EandE/Web_sites/14-15/XL_Monopiles/ (Accessed: 7 September 2017).
[22] Schijve J. Fatigue of structures and materials. 2nd ed Springer Science + Business Media, B.V; 2009. p. 241 Available at: DOI:10.15713/ins.mmj.3.
[23] Bhattacharya S. Challenges in design of foundations for offshore wind turbines. Eng Technol Ref 2014:1–9. https://doi.org/10.1049/etr.2014.0041.
[24] Andersen LV, Vahdatirad MJ, Sichani MT, Sørensen JD. Natural frequencies of wind turbines on monopile foundations in clayey soils—A probabilistic approach. Comput Geotech 2012;43:1–11. https://doi.org/10.1016/j.compgeo.2012.01.010.
[25] Adhikari S, Bhattacharya S. Dynamic analysis of wind turbine towers on flexible foundations. Shock Vib 2012;19(1):37–56. https://doi.org/10.3233/SAV-2012-0615.
[26] Igwemezie Victor, Mehmanparast Ali, Kolios Athanasios. Materials selection for XL wind turbine support structures: a corrosion-fatigue perspective. Mar Struct 2018;61:381–97. https://doi.org/10.1016/j.marstruc.2018.06.008.
[27] Barsom JM, Rolfe ST. Fracture and fatigue control in structures : applications of fracture mechanics. 3rd ed. ASTM; 1999. p. 318–23 Available at: DOI:10.1520/MNL41-3RD-EB.
[28] de Jesus Abílio MP, Matos Rui, Fontoura Bruno FC, Rebelo Carlos, Simões da Silva Luis, Veljkovic Milan. A comparison of the fatigue behavior between S355 and S690 steel grades. J Constr Steel Res 2012;79:140–50. https://doi.org/10.1016/j.jcsr.2012.07.021.
[29] Atkinson JD, Lindley TC. Effect of stress waveform and hold-time on environmentally assisted fatigue crack propagation inC-Mn structural steel. Metal Sci 1979;13(7):444–8. https://doi.org/10.1179/msc.1979.13.7.444.
[30] Musuva JK. Fatigue crack growth in a low-alloy steel. University of London; 1980. Available at: https://spiral.imperial.ac.uk/bitstream/10044/1/35278/2/Musuva-JK-1980-PhD-Thesis.pdf (Accessed: 27 September 2018).
[31] Achilles RD, Bulloch JH. The influence of waveform on the fatigue crack growth behaviour of SA508 cl III RPV steel in various environments. Int J Press Vessels Pip 1987;30(5):375–89. https://doi.org/10.1016/0308-0161(87)90110-4.
[32] Barsom JM. Corrosion-fatigue crack propagation below. Eng Fract Mech 1971;3(1):15–25. https://doi.org/10.1016/0013-7944(71)90048-8.
[33] Musuva JK, Radon JC. The effect of stress ratio and frequency on fatigue crack growth. Fat Frac Eng Mat Struct 1979;1(4):457–70. https://doi.org/10.1111/ffe.1979.1.issue-410.1111/j.1460-2695.1979.tb01333.x.
[34] Vestas Wind Systems A/S. Vestas V120 4.5 MW wind turbine. Denmark; 2005. Available at: http://www.nrg-systems.hu/dok/en/V120_UK.pdf.
[35] Bhattacharya Subhamoy, Cox James A, Lombardi Domenico, Muir Wood David. Dynamics of offshore wind turbines supported on two foundations. Proc Inst Civil Eng - Geotechn Eng 2013;166(2):159–69. https://doi.org/10.1680/geng.11.00015.
[36] Bak C, Zahle F, Bitsche R, Yde A, Henriksen LC, Nata- A, et al. Description of the DTU 10 MW reference wind turbine department of wind energy I-report. 2013. Available at: https://dtu-10mw-rwt.vindenergi.dtu.dk.
[37] Yu Lu-Qing, Wang Li-Zhong, Guo Zhen, Bhattacharya S, Nikitas G, Li Ling-Ling, Xing Yue-Long. Long-term dynamic behavior of monopile supported offshore wind turbines in sand. Theor Appl Mech Lett 2015;5(2):80–4. https://doi.org/10.1016/j.taml.2015.02.003.
[38] Igwemezie V, Dirisu P, Mehmanparast A. Critical assessment of the fatigue crack growth rate sensitivity to material microstructure in ferrite-pearlite steels in air and marine environment. Mater Sci Eng, A 2019;754:750–65.
[39] Austen IM. Quantitative understanding of corrosion fatigue crack growth behaviour. Luxembourg; 1983.
[40] Smiths Metal Centres. EN24 Engineering Steel. 2019. pp. 1–3. Available at: https://www.smithmetal.com/en24.htm (Accessed: 27 December 2019).
[41] Express Steel. EN24T Engineering Steel, EN24 Steel treated in the T condition. Steel Express Ltd. 2019. pp. 1–5. Available at: steelexpress.co.uk/engineeringsteel/EN24T.html (Accessed: 27 December 2019).
[42] Metal Suppliers Online. 300M alloy steels material property data sheet. 2019. pp. 1–4. Available at: suppliersonline.com/propertypages/300M.asp.
[43] SteelJIS. JIS SNCM439 - Datasheet, chemical composition, standards and properties. 2019. Available at: steeljis.com/jis_steel_datasheet.php?name_id = 43 (Accessed: 27 December 2019).
[44] Bhuyan GS, Swamidas ASJ, Vosikovsky O. Influence of environmental and mechanical variables on fatigue crack growth rates in CSA G40.21M 350 WT steel. Int J Fatigue 1988;10(1):37–42.
[45] Chapel Steel Corp. Structural, carbon & HSLA steel plate. 2018. pp. 1–5. Available at: https://www.chapelsteel.com/csa-g4021-50w-50a.html (Accessed: 27 December 2019).
[46] Appleton RJ. Corrosion fatigue of a C-Mn steel, PhD Thesis. Department of Mechanical Engineering, University of Glasgow; 1985. Available at: http://theses.gla.ac.uk/2176/ (Accessed: 13 February 2018).
[47] Corus Construction & Industrial. European structural steel standard EN 10025 : 2004. 2004. Available at: http://www.tf.uni-kiel.de/matwis/amat/iss/kap_9/articles/en_steel_standards.pdf (Accessed: 5 April 2016).
[48] Gray RA, Hawthorne JR. Mechanical properties behavior of neutron irradiated 12Ni-5Cr-3Mo maraging steel plate and companion weld metal. Nucl Eng Des 1970;11:381–92.
[49] Barsom J. Fatigue crack growth under variable amplitude loading in various bridge steels. Fatigue crack growth under spectrum loads. ASTM STP 595. 1976;217–35.
[50] Wang ZF, Li J, Wang JQ, Ke W. The influence of loading waveform on corrosion fatigue crack propagation. Corros Sci 1995;37(10):1551–65.
[51] Knop M, Birbilis N, Lynch S. Effects of waveform and cycle period on corrosion-fatigue crack growth in cathodically protected high-strength steels. Adv Mater Res 2014;891–892:211–6. https://doi.org/10.4028/www.scientific.net/AMR.891-892.211.
[52] Steel International T. New Horizons - supply solutions in offshore structual steel. 2010. Available at: http://www.tatasteeleurope.com/static_files/StaticFiles/Business_Units/International/Tata Steel International Offshore Capability 2010.pdf (Accessed: 5 April 2016).
[53] ASTM. ASTM E647-15: Standard test method for measurement of fatigue crack growth rates. 2015. Available at: DOI:10.1520/E0647-15.2.
[54] Slezak T., Sniezek L. A comparative LCF study of S960QL high strength steel and S355J2 mild steel. Procedia Engineering. 2015; 114: 78–85. Available at: https://ac.els-cdn.com/S1877705815016835/1-s2.0-S1877705815016835-main.pdf?_tid = a64b914d-b256-4bf1-bca8-3f2ab3afd688&acdnat = 1547527288_d017f7cfa2d300a96252b52d0e7c49c9 (Accessed: 15 January 2019).
[55] BSI Standards. BS 7910:2013 + A1: Guide to methods for assessing the acceptability of flaws in metallic structures. BSI Standards. 2015.
[56] ASTM. D1141-98 Standard practice for the preparation of substitute ocean water. Astm. 2013; 98(Reapproved): 1–3. Available at: DOI:10.1520/D1141-98R13.2.
[57] Adedipe O, Brennan F, Kolios A. Corrosion fatigue load frequency sensitivity analysis. Mar Struct 2015;42:115–36. https://doi.org/10.1016/j.marstruc.2015.03.005.
[58] Vishay., Vishay M-M. Model P3 strain indicator and recorder. 2005; (March). Available at: http://www.vishaypg.com/micro-measurements/.
[59] Vishay. Application of M-Coat J protective coating instruction bulletin B-147-5. 2015.
[60] Instron. Intelligent software for fatigue and dynamic testing. Available at: www.

instron.com.
[61] BSI. BS EN ISO 11782-2:2008: Corrosion of metals and alloys — Corrosion fatigue testing —Part 2: Crack propagation testing using precracked specimens. British Standard. 2008.
[62] Adedipe O. Integrity of offshore structures. Cranfield University; 2015.
[63] Dhinakaran S, Prakash Raghu V. Effect of low cyclic frequency on fatigue crack growth behavior of a Mn–Ni–Cr steel in air and 3.5% NaCl solution. Mater Sci Eng, A 2014;609:204–8. https://doi.org/10.1016/j.msea.2014.05.001.
[64] Gill SJ, Crooker TW. Fatigue crack propagation in an HSLA Steel (MF-80). Air and in Salt Water Mar Technol 1990;27(4):221–4.
[65] Tamura I, Sekind H, Taanaka T, Ouchi C. Thermomechanical processing of high-strength low-alloy steels. Butterworths; 1988. p. 248.
[66] Korda Akhmad A, Mutoh Y, Miyashita Y, Sadasue T, Mannan SL. In situ observation of fatigue crack retardation in banded ferrite–pearlite microstructure due to crack branching. Scr Mater 2006;54(11):1835–40. https://doi.org/10.1016/j.scriptamat.2006.02.025.